



A Sub-Neptune-sized Planet Transiting the M2.5 Dwarf G 9-40: Validation with the Habitable-zone Planet Finder

Gudmundur Stefansson^{1,2,3,4,21,22} , Caleb Cañas^{1,2,3,21} , John Wisniewski⁵ , Paul Robertson⁶ , Suvrath Mahadevan^{1,2,3} , Marissa Maney¹, Shubham Kanodia^{1,2} , Corey Beard⁶, Chad F. Bender⁷ , Peter Brunt⁸, J. Christopher Clemens⁹, William Cochran¹⁰ , Scott A. Diddams^{11,12}, Michael Endl¹⁰ , Eric B. Ford^{1,2,3,13} , Connor Fredrick^{11,12}, Samuel Halverson^{14,23} , Fred Hearty^{1,2}, Leslie Hebb¹⁵ , Joseph Huehnerhoff¹⁶, Jeff Jennings^{11,12}, Kyle Kaplan⁷, Eric Levi¹, Emily Lubar¹, Andrew J. Metcalf^{11,12,17}, Andrew Monson¹, Brett Morris¹⁶ , Joe P. Ninan^{1,2} , Colin Nitroy¹, Lawrence Ramsey^{1,2,3}, Arpita Roy^{18,24} , Christian Schwab¹⁹ , Steinn Sigurdsson^{1,2,3} , Ryan Terrien²⁰ , and Jason T. Wright^{1,2,3} 

¹ Department of Astronomy & Astrophysics, The Pennsylvania State University, 525 Davey Lab, University Park, PA 16802, USA; gstefansson@astro.princeton.edu

² Center for Exoplanets & Habitable Worlds, University Park, PA 16802, USA

³ Penn State Astrobiology Research Center, University Park, PA 16802, USA

⁴ Department of Astrophysical Sciences, Princeton University, 4 Ivy Lane, Princeton, NJ 08540, USA

⁵ Homer L. Dodge Department of Physics and Astronomy, University of Oklahoma, 440 W. Brooks Street, Norman, OK 73019, USA

⁶ Department of Physics and Astronomy, University of California-Irvine, Irvine, CA 92697, USA

⁷ Steward Observatory, University of Arizona, Tucson, AZ 85721, USA

⁸ AVR Optics, 187 North Water Street, Rochester, NY 14604, USA

⁹ University of North Carolina at Chapel Hill, Chapel Hill, NC 27599, USA

¹⁰ Department of Astronomy and McDonald Observatory, University of Texas at Austin, 2515 Speedway, Stop C1400, Austin, TX 78712, USA

¹¹ Time and Frequency Division, National Institute of Standards and Technology, 325 Broadway, Boulder, CO 80305, USA

¹² Department of Physics, University of Colorado, 2000 Colorado Avenue, Boulder, CO 80309, USA

¹³ Institute for CyberScience, The Pennsylvania State University, 525 Davey Laboratory, University Park, PA 16802, USA

¹⁴ MIT Kavli Institute for Astrophysics, 70 Vassar St, Cambridge, MA 02109, USA

¹⁵ Department of Physics, Hobart and William Smith Colleges, 300 Pulteney Street, Geneva, NY 14456, USA

¹⁶ Department of Astronomy, Box 351580, University of Washington, Seattle, WA 98195, USA

¹⁷ Space Vehicles Directorate, Air Force Research Laboratory, 3550 Aberdeen Ave SE, Kirtland AFB, NM 87117, USA

¹⁸ California Institute of Technology, 1200 E California Blvd, Pasadena, CA 91125, USA

¹⁹ Department of Physics and Astronomy, Macquarie University, Balaclava Road, North Ryde, NSW 2109, Australia

²⁰ Department of Physics and Astronomy, Carleton College, Northfield, MN 55057, USA

Received 2019 July 8; revised 2019 October 29; accepted 2019 November 29; published 2020 February 12

Abstract

We validate the discovery of a 2-Earth-radii sub-Neptune-sized planet around the nearby high-proper-motion M2.5 dwarf G 9-40 (EPIC 212048748), using high-precision, near-infrared (NIR) radial velocity (RV) observations with the Habitable-zone Planet Finder (HPF), precision diffuser-assisted ground-based photometry with a custom narrowband photometric filter, and adaptive optics imaging. At a distance of $d = 27.9$ pc, G 9-40b is the second-closest transiting planet discovered by *K2* to date. The planet's large transit depth (~ 3500 ppm), combined with the proximity and brightness of the host star at NIR wavelengths ($J = 10$, $K = 9.2$), makes G 9-40b one of the most favorable sub-Neptune-sized planets orbiting an M dwarf for transmission spectroscopy with *James Webb Space Telescope*, ARIEL, and the upcoming Extremely Large Telescopes. The star is relatively inactive with a rotation period of ~ 29 days determined from the *K2* photometry. To estimate spectroscopic stellar parameters, we describe our implementation of an empirical spectral-matching algorithm using the high-resolution NIR HPF spectra. Using this algorithm, we obtain an effective temperature of $T_{\text{eff}} = 3404 \pm 73$ K and metallicity of $[\text{Fe}/\text{H}] = -0.08 \pm 0.13$. Our RVs, when coupled with the orbital parameters derived from the transit photometry, exclude planet masses above $11.7M_{\oplus}$ with 99.7% confidence assuming a circular orbit. From its radius, we predict a mass of $M = 5.0^{+3.8}_{-1.9}M_{\oplus}$ and an RV semi-amplitude of $K = 4.1^{+3.1}_{-1.6}$ m s⁻¹, making its mass measurable with current RV facilities. We urge further RV follow-up observations to precisely measure its mass, to enable precise transmission spectroscopic measurements in the future.

Unified Astronomy Thesaurus concepts: Exoplanet astronomy (486); Exoplanet systems (484); Radial velocity (1332); Exoplanet detection methods (489); Transit photometry (1709); Low mass stars (2050); Mini Neptunes (1063); Exoplanets (498)

Supporting material: data behind figure, machine-readable table

1. Introduction

Surveying the ecliptic plane, the *K2* mission (Howell et al. 2014) has expanded on the exoplanet discoveries of the original

Kepler (Borucki et al. 2010) mission. In particular, *K2* has sampled a different population of planet hosts than *Kepler*, namely detecting planets orbiting brighter and closer stars, and stars of later spectral type. Among these, planets around bright, nearby M dwarfs are compelling targets for further characterization for many reasons.

First, planets around bright M dwarfs are amenable to precision radial velocity (RV) observations—especially for

²¹ NASA Earth and Space Science Fellow.

²² Henry Norris Russell Fellow.

²³ NASA Sagan Fellow.

²⁴ Millikan Prize Postdoctoral Fellow.

Doppler spectrographs operating in the near-infrared (NIR)—to measure their masses and to search for additional planets. Measuring their masses will help shed light on the exoplanet mass–radius (MR) relation (Weiss & Marcy 2014; Wolfgang et al. 2016; Chen & Kipping 2017; Ning et al. 2018) of planets around M dwarfs. Recent work by Kanodia et al. (2019), comparing the exoplanet MR relation of M dwarf planets to that of the *Kepler* sample of earlier-type planet hosts hints at a difference between the resulting MR relationships. However, the comparison is still heavily influenced by the seven TRAPPIST-1 planets, which account for $\sim 30\%$ of known M dwarf planets with precisely determined masses and radii. To confirm if there is a statistical difference in the MR relationship between M dwarf planets and earlier-type planets, we need to increase the number of transiting M dwarf planets with precisely measured masses.

Second, the large planet-to-star radius ratios of planets orbiting M dwarfs make them favorable targets for transmission spectroscopy with upcoming facilities, such as *James Webb Space Telescope* (*JWST*; Cowan et al. 2015), *ARIEL* (Tinetti et al. 2016), and the Extremely Large Telescopes (ELTs). A precise measurement of the planetary mass is a requirement for inference of atmospheric features to disentangle degeneracies that exist between the atmospheric scale height and the mean molecular weight of the atmosphere (Batalha et al. 2017). Although recent studies (e.g., Crossfield & Kreidberg 2017) have demonstrated rising statistical trends that show cold ($T_{\text{eq}} < 800$ K) sub-Neptune-sized planets tend to have damped transmission spectroscopic features, sub-Neptune-sized planets have no analog in the solar system, making them particularly interesting targets as they are observed to have a diverse range of compositions and observed radii (e.g., Fulton et al. 2017), resulting in a diverse range of possible atmospheres.

In this paper, we validate the planetary nature of an $R \sim 2.0R_{\oplus}$ sub-Neptune-sized planet orbiting the nearby high-proper-motion M2.5 dwarf star G 9-40, also known as EPIC 212048748, NLTT 20661, 2MASS J08585232+2104344, and *Gaia* DR2 684992690384102528. At a distance of $d = 27.9$ pc, G 9-40b is currently the second-closest planetary system discovered by the *K2* mission. G 9-40b was originally identified as a planet candidate in *K2* Campaign 16 by Yu et al. (2018), and here we perform the necessary observations to validate the planet candidate as a bona fide planet through precision ground-based diffuser-assisted transit photometry using the Astrophysical Research Consortium Telescope Imaging Camera (ARCTIC; Huehnerhoff et al. 2016) on the Astrophysical Research Consortium (ARC) 3.5 m Telescope at Apache Point Observatory, adaptive optics imaging using the ShaneAO instrument (Srinath et al. 2014) on the 3 m Shane Telescope at Lick Observatory, and precision NIR radial velocities obtained with the Habitable-zone Planet Finder (HPF) Spectrograph (Mahadevan et al. 2012, 2014). Using the HPF NIR spectra, we provide precise spectroscopic parameters using an empirical spectral-matching technique and use the spectra for precision velocimetry to provide an upper bound on the mass of G 9-40b.

The paper is structured as follows. In Section 2 we discuss the observations used in this paper. We discuss our best estimates of the stellar parameters of the host star in Section 3, describing our implementation of an empirical spectral-matching algorithm closely following the popular *SpecMatch-emp* algorithm from Yee et al. (2017). In Section 4 we discuss the transit analysis of the *K2* and ground-based data and

the resulting best-fit planet parameters. In Section 5 we discuss our false-positive analysis using the VESPA statistical validation tool, where we statistically validate G 9-40b as a planet. In Section 6 we compare G 9-40b to other known planetary systems and provide a further discussion of the feasibility for future study of this system through transmission spectroscopy and precision RV observations. Finally, we conclude the paper in Section 7 with a summary of our key results.

2. Observations

2.1. *K2* Photometry

G 9-40 was observed by the *Kepler* spacecraft as part of Campaign 16 of the *K2* mission. It was proposed as a *K2* Campaign 16 target by the following programs: GO16005_LC (PI: Crossfield), GO16009_LC (PI: Charbonneau), GO16052_LC (PI: Stello), and GO16083_LC (PI: Coughlin). The star was monitored in long cadence mode (30 minute cadence) for 80 days from 2017 December 7 to 2018 February 25 and was originally identified as a candidate planet host by Yu et al. (2018). We used the *Everest* pipeline (Luger et al. 2016, 2018) to detrend and correct for photometric variations seen in the *K2* photometry that are due to imperfect pointing of the spacecraft with only two functioning reaction wheels. The unbinned 6.5 hr photometric precision before detrending was 193 ppm, and it decreased to 30 ppm after detrending with *Everest*.

2.2. High-resolution Doppler Spectroscopy

We obtained four visits of G 9-40 with the HPF Spectrograph with the goal to measure its RV variation as a function of time. HPF is a high-resolution ($R \sim 55,000$) NIR spectrograph recently commissioned on the 10 m Hobby–Eberly Telescope (HET) in Texas covering the information-rich z , Y , and J bands from 810 to 1280 nm (Mahadevan et al. 2012, 2014). HPF is actively temperature stabilized, achieving ~ 1 mK temperature stability long term (Stefansson et al. 2016). The HET is a fully queue-scheduled telescope with all observations executed in a queue by the HET resident astronomers (Shetrone et al. 2007). In each visit, we obtained two 945 s exposures, yielding a total of eight spectra with a median signal-to-noise ratio (S/N) of 123 per extracted 1D pixel at $\lambda = 1000$ nm.

HPF has an NIR laser-frequency comb (LFC) calibrator that has been shown to enable ~ 20 cm s^{-1} calibration precision and 1.53 m s^{-1} RV precision on sky on the bright and stable M dwarf Barnard’s Star (Metcalf et al. 2019). We elected to not use the simultaneous LFC reference calibrator for these observations to minimize any possibility of scattered LFC light in the target spectrum. Instead, the drift correction was performed by extrapolating the wavelength solution from other LFC exposures from the night of the observations. As discussed in detail in the Appendix, HPF’s nightly drift is a predictable linear sawtooth pattern with a 10–15 m s^{-1} amplitude (see Figure 14 in Appendix), where dedicated LFC calibration exposures are generally taken nightly a few hours apart, enabling precise wavelength calibration even without simultaneous LFC calibration exposures (Metcalf et al. 2019). To further illustrate this linear behavior, in the Appendix, we show the LFC drift exposures for the four nights we obtained G 9-40 observations. Lastly, in the Appendix, we also estimate the error contribution of the drifts to the total RV errors using a leave-one approach. In doing so, we estimate errors at the

$<30 \text{ cm s}^{-1}$ level for our G 9-40 observations, which we add in quadrature to the errors estimated from our RV extraction (see Table 6).

The HPF 1D spectra were reduced and extracted with the custom HPF data-extraction pipeline following the procedures outlined in Ninan et al. (2018), Kaplan et al. (2018), and Metcalf et al. (2019). After the 1D spectral extraction, we extracted precise NIR RVs using a modified version of the SpEctrum Radial Velocity Analyzer (SERVAL) pipeline (Zechmeister et al. 2018) following the methodology discussed in Metcalf et al. (2019). In short, SERVAL uses a template-matching technique to derive RVs (see Anglada-Escudé & Butler 2012; Zechmeister et al. 2018). This technique relies on minimizing the differences of the observed spectrum against a high-S/N master template constructed from a coaddition of all available observations of the target star. We generated the master template by performing a best-fit spline regression to the eight as-observed spectra of the target star. Following the methodology described in Metcalf et al. (2019), we masked out all telluric and sky-emission line regions, using a thresholded synthetic telluric-line mask and an empirical thresholded sky-emission line mask, respectively. We generated the telluric-line mask using the `teffit` (Gullikson et al. 2014) Python wrapper to the Line-by-Line Radiative Transfer Model package (LBLRTM; Clough et al. 2005). For the sky-emission line mask, we used the same empirical blank-sky sky-emission line mask as used in Metcalf et al. (2019). We calculated the barycentric corrections using the `barycorrpy` Python package (Kanodia & Wright 2018), which uses the barycentric-correction algorithms from Wright & Eastman (2014).

2.3. Adaptive Optics Imaging

To constrain contamination from background sources and study the possibility that astrophysical false positives could be the source of the transits (e.g., eclipsing binaries or background eclipsing binaries), we performed high-contrast adaptive optics (AO) imaging of G 9-40 using the 3 m Shane Telescope at Lick Observatory on 2018 November 25. We performed the AO imaging using the upgraded ShARCS camera (Srinath et al. 2014) in the K_s bandpass. We observed the star using a five-point dither pattern (see, e.g., Furlan et al. 2017), imaging the star at the center of the detector and in each quadrant. Individual images had an exposure time of 30 s, and we obtained a total of 20 minutes of integration time across all exposures.

Standard image processing (e.g., flat-fielding, sky subtraction), as well as subpixel image alignment, was performed using custom Python software. Using the combined image, we computed the variance in flux in a series of concentric annuli centered on the target star. The resulting 5σ contrast curve is shown in Figure 1. From the images we see that no bright ($\Delta K_s < 4$) secondary companions are detectable within $0''.5$. These data show that there is no evidence of blending up to a radius of $2''.5$. We therefore infer that the transits observed from both *K2* and from the ground (see Section 4) are not contaminated by background sources.

2.4. Seeing-limited Imaging

To constrain blends within the *K2* aperture at distances farther than the $2''.5$ field of view (FOV) of the diffraction-limited Lick/ShaneAO images shown in Figure 1, we obtained

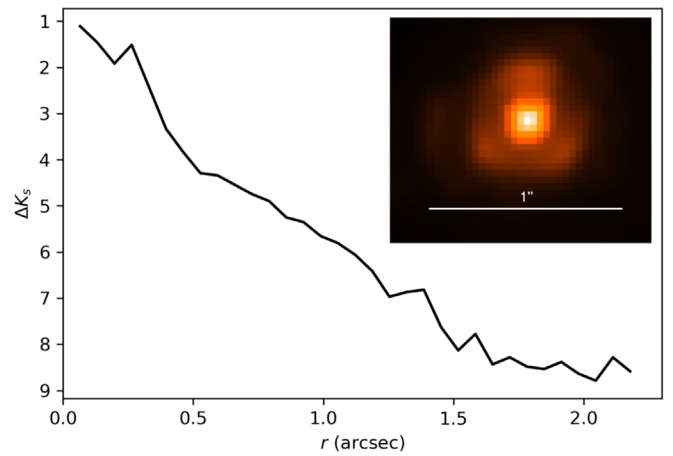


Figure 1. Adaptive optics K_s band contrast curve (azimuthally averaged) of G 9-40 from ShARCS on the Shane 3 m Telescope. No bright companions are seen to within $0''.5$ separation. The inset image shows the as-observed AO image along with a $1''$ bar for scale.

seeing-limited images using the ARCTIC imager (Huehnerhoff et al. 2016) on the 3.5 m Astrophysical Research Consortium Telescope (Figure 2(b)). On the night of 2019 January 14, we obtained 20 seeing-limited images of G 9-40 using an exposure time of 10 s in the Sloan Digital Sky Survey (SDSS) g' filter. The skies were photometric with a seeing of $0''.75$. We median combined the full set of 20 images to create a high-S/N final image shown in Figure 2. Given G 9-40's high proper motion, we compare our median-combined seeing-limited image to archival observations from the POSS1 survey obtained using the `astroquery skyview` service (Ginsburg et al. 2018) in Figure 2. The POSS1 image shows no evidence for a background star at G 9-40's current coordinates marked by the yellow circle ($7''$ radius) in both panels in Figure 2. In addition to this, we also queried the *Gaia* archive (Gaia Collaboration 2018) for nearby sources. In doing so, *Gaia* reveals one companion at a distance of $20''$ from G 9-40, with a $\Delta G = 5$, that is both significantly fainter than G 9-40 and outside the *K2* aperture. Given G 9-40's proper motion of $\mu_\alpha = 175 \text{ mas yr}^{-1}$ and $\mu_\delta = -318 \text{ mas yr}^{-1}$ and the short time span between the *Gaia* and *K2* observations, we conclude that this star is not a significant source of dilution in the *K2* and diffuser-assisted transits.

2.5. Diffuser-assisted Photometry from the ARC 3.5 m

We observed the transit of G 9-40b using the ARCTIC imager (Huehnerhoff et al. 2016) on the ARC 3.5 m Telescope at Apache Point Observatory on the night of 2019 April 13 local time (04:50 UT–07:30 UT April 14). The night was photometric with a seeing of $\sim 0''.75$ at the beginning of the night. The target rose from air mass 1.55 to air mass 1.05 during the observations.

We observed the transit using the Engineered Diffuser on the ARCTIC imager, which has been described in detail in Stefansson et al. (2017, 2018a). In short, the Engineered Diffuser molds the focal-plane image of the star into a broad and stable top-hat shape, allowing us to increase our exposure times to gather more photons per exposure while minimizing correlated errors due to point-spread function variations and guiding errors. The increased exposure time allows us to further average over scintillation errors by increasing the duty cycle of the observations (Stefansson et al. 2017). We used a newly

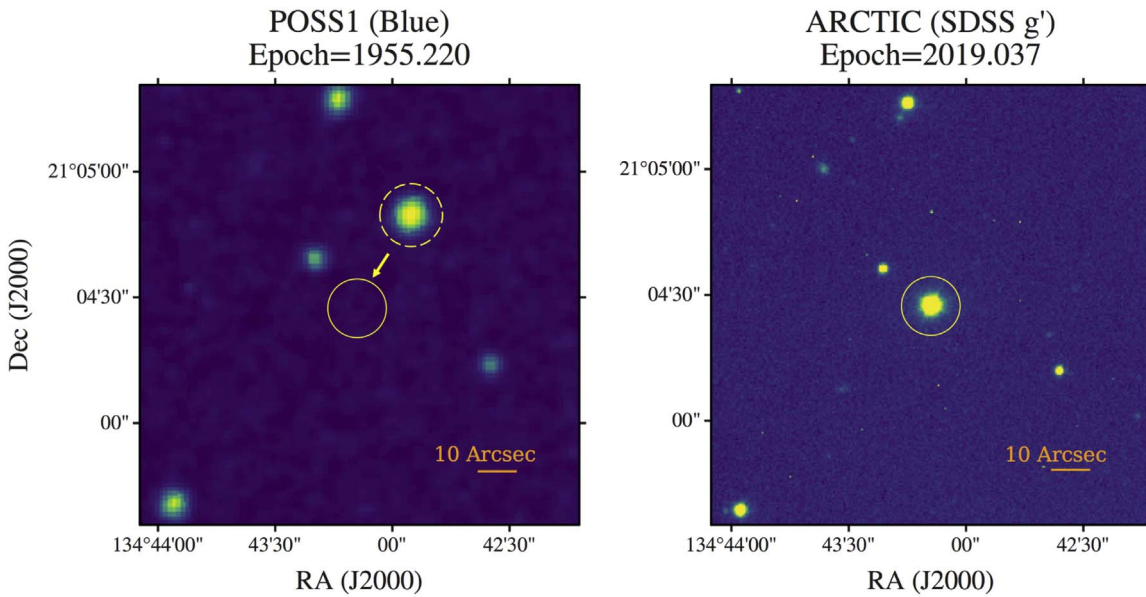


Figure 2. (a) Seeing-limited image of G 9-40 obtained by POSS1 in the blue filter from the Digital Sky Survey-1 (DSS-1) from 1955. (b) Seeing-limited image using the ARCTIC imager on the 3.5 m ARC Telescope at Apache Point Observatory in the SDSS g' filter from our 2019 observations. The filled yellow circle ($7''$ radius) denotes the position of G 9-40 at epoch 2019.037, and the dashed yellow circle in panel (a) highlights the position of G 9-40 at the epoch of the POSS1 plate (1955.22). From the POSS1 image we see that no background star is visible at the position of G 9-40 during the ARCTIC and the *K2* transit observations. This suggests that G 9-40 is the true source of the transits. North is up, and east is to the left.

commissioned, custom-fabricated narrowband filter from AVR Optics²⁵ and Semrock Optics,²⁶ centered on 857 nm with a 37 nm width in a region with minimal telluric absorption. The filter, along with its as-measured throughput curve, has been further discussed in Stefansson et al. (2018b). The filter is 5 inches in diameter, covering the full ARCTIC beam footprint in the optical path, resulting in minimal vignetting and allowing the observer to make use of the full field of view (FOV) of ARCTIC. The combination of the Engineered Diffuser and the narrowband filter allowed us to make use of a bright reference star HD 76780 ($V = 7.63$, $I = 6.7$; G 9-40 has an SDSS i' magnitude of 11.994) within the FOV at a high observing efficiency of 76.9% with a cadence of 18.2 s between successive exposures (exposure time of 14 s).²⁷

We reduced the on-sky transit observations along with the 25 bias and 25 dome flat-field calibration frames using Astro-ImageJ (Collins et al. 2017) following the methodology in Stefansson et al. (2017). We calculate the Barycentric Julian Date (BJD_{TDB}) time using the Python package *barycorrpy*. After experimenting with different aperture radii and annuli, we found that the aperture setting that yielded the smallest residuals was a value of 30 pixels ($6''.9$) for the target star aperture, 40 pixels ($9''.2$) for the inner annulus, and 80 pixels ($18''.4$) for the outer annulus for background estimation. This resulted in peak ADU/pixel counts of ~ 1000 and $\sim 42,900$ for the target and reference star, respectively. After removing the best-fit transit model and six additional significant ($>3\sigma$) outliers present in the data, we obtained an unbinned precision of 1225 ppm, which is further discussed in Section 4. The transit is shown in Figure 7, where the data are shown with

error bars estimated following the methodology in Stefansson et al. (2017) and accounting for errors from photon, dark, read, background, digitization, and scintillation noise.

3. Stellar Parameters

3.1. Stellar Parameters from Matching to an Empirical Library of Spectra

In this subsection, we discuss our implementation of the *SpecMatch-Emp* algorithm described in Yee et al. (2017) to derive precise estimates of the spectroscopic effective temperature (T_{eff}), metallicity ($[\text{Fe}/\text{H}]$), and surface gravity ($\log g$) of G 9-40 through comparing our high-resolution NIR HPF spectra of G 9-40 to a library of high-S/N as-observed HPF spectra with well-characterized stellar parameters. As this is the first description of this implementation for this algorithm for HPF spectra, we provide an initial description here on its performance. As we assemble a larger HPF spectral library, we plan to further detail the performance and applicability of this algorithm on the larger high-resolution NIR M dwarf library. In the next subsections we further discuss our spectral library, the algorithm, and its performance in recovering the stellar parameters of the stars internal to the library using a cross-calibration scheme. We then discuss our best-estimate stellar parameter values of G 9-40, and finally we discuss future work we plan to perform to further improve the performance of the code framework described here.

3.1.1. Spectral Library

We assembled a spectral library of high-S/N as-observed HPF spectra that compose a subsection of the library stars in the *SpecMatch-Emp* code from Yee et al. (2017), all of which have precisely characterized stellar parameters. We restrict our library to a subsection of the stars from Yee et al. (2017) that have an effective temperature of $T_{\text{eff}} < 4000$ K.

²⁵ <http://avr-optics.com/>

²⁶ <https://www.semrock.com/>

²⁷ To further minimize readout time and maximize our observing efficiency, we used ARCTIC in the 2×2 quad-amplifier binning mode (gain of $1.97 \text{ e}^-/\text{ADU}$, read noise of 6.7 e^-) with a readout time of 4.2 s.

Our current library consists of 26 stars, where all of the spectra have an S/N > 162 with a median S/N of 495 evaluated at $\sim 1.1 \mu\text{m}$. The current library covers the following parameter ranges: $3080 \text{ K} < T_{\text{eff}} < 3989 \text{ K}$, $4.63 < \log(g) < 5.11$, and $-0.49 < [\text{Fe}/\text{H}] < 0.4$.

To generate the stellar library, we performed a first-order deblaze correction of the HPF science and the sky calibration fibers using the dedicated HPF flat-field lamp. We then subtracted the deblaze-corrected sky contamination from the science fiber light to minimize the impact of sky-background and sky-emission lines on the determination of the spectral parameters. To ensure that all of the relevant spectral features line up for the spectral comparison, we shifted the spectra first to the barycenter of the solar system using the `barycorrpy` package, and we subsequently shifted the spectrum to the stellar rest frame by fitting for the best-fit absolute RV value by fitting a Gaussian to the cross-correlation function (CCF) with a reference binary mask. The CCF binary mask is the same mask we used to calculate the absolute RV of G 9-40, as detailed in Section 3.3. After correcting for both Doppler shifts, we then resampled the spectra using linear interpolation onto a common wavelength grid with a fixed 0.01 Å spacing—about four times smaller than the smallest pixel spacing in HPF to minimize any information loss in the interpolation step—to facilitate the χ^2 comparison. For the parameter retrieval, we experimented using six different HFP orders that were relatively clean of telluric absorption lines for the parameter retrieval, all of which returned consistent stellar parameters. This comparison is further described in Section 3.1.3.

3.1.2. Empirical SpecMatch Algorithm

Following Yee et al. (2017), we use a χ^2 metric to compare the goodness of fit of a target spectrum S_{target} to a given $S_{\text{reference}}$ star spectrum in the spectral library,

$$\chi_{\text{initial}}^2 = \sum_{i=1}^N (S_{\text{target},i} - S_{\text{reference},i}(p, v \sin i))^2, \quad (1)$$

where $S_{\text{target},i}$ is the deblazed and normalized flux of the target star, and $S_{\text{reference},i}(p, v \sin i)$ is the deblazed and normalized flux of the library reference star at the i th element of the resampled wavelength array (N in total). We rotationally broadened the reference star flux, $S_{\text{reference},i}(p, v \sin i)$, by a projected rotational velocity $v \sin i$ and multiplied by a fifth-order Chebyshev polynomial denoted by the six-element vector p to remove any low-order residual variations in the deblazed spectra. For the $v \sin(i)$ rotational broadening, we adopt the broadening kernel from Gray (1992), following the implementation in Yee et al. (2017). Following Yee et al. (2017), we specifically do not scale the χ^2 value in Equation (1) by the estimated photon-noise error bars, as the residuals of the high-S/N spectra are completely dominated by systematic astrophysical or instrumental differences rather than our estimate of the photon noise. Using the χ^2 metric from Equation (1), we loop through all of the spectra in the library to optimize for a minimum χ^2 value as a function of the Chebyshev polynomial vector p and $v \sin i$. We used the Nelder-Mead simplex (“*Amoeba*”) algorithm (Nelder & Mead 1965) as implemented in the `scipy.optimize` package. Following Yee et al. (2017), we enforce a limited range of allowed $v \sin i$ values

between 0 km s^{-1} (no broadening) and 15 km s^{-1} to minimize excursions to artificially high $v \sin i$ values.

Following the χ_{initial}^2 loop, we then select the top five lowest- χ_{initial}^2 spectra to form a new composite spectrum, $S_{\text{composite}} = \sum_{j=1}^5 c_j S_j(p_j, [v \sin i]_j)$, where the five coefficients $c = \{c_1, c_2, c_3, c_4, c_5\}$ are optimized to further minimize the χ^2 of the target star and the composite spectrum according to the following χ^2 metric:

$$\chi_{\text{composite}}^2 = \sum_{i=1}^N \left(S_{\text{target},i} - \sum_{j=1}^5 c_j S_{j,i}(p_j, [v \sin i]_j) \right)^2, \quad (2)$$

where p_j and $[v \sin i]_j$ are the best-fit values determined from the optimization step in Equation (1) for the j th best reference spectrum ($j \in \{1, 2, \dots, 5\}$). We fit for the first four c coefficients in the optimization step and then set

$$c_5 = 1 - \sum_{j=1}^4 c_j \quad (3)$$

to ensure that all five coefficients sum up to unity. All of the c coefficients are further constrained to have a value between 0 and 1.

3.1.3. Cross-validation

To check the performance of the algorithm described above on the NIR HPF spectra, we performed a cross-validation procedure consisting of removing a given spectrum from the library and comparing the recovered best-fit stellar parameter to its known library value. We then repeated this comparison for all of the stars in the library, and we computed the standard deviation (σ) of the residuals between the recovered best-fit stellar parameters and the known library value for the three stellar parameters considered (i.e., computing $\sigma_{T_{\text{eff}}}$, $\sigma_{\text{Fe}/\text{H}}$, and $\sigma_{\log g}$). To compare the performance of different HPF orders in recovering the known parameter values, we ran this cross-validation procedure on six different HPF orders that are relatively clean of telluric absorption features. Table 1 summarizes the comparison between the different orders, showing the resulting $\sigma_{T_{\text{eff}}}$, $\sigma_{\text{Fe}/\text{H}}$, and $\sigma_{\log g}$ values. From Table 1, we see that the different orders overall show similar scatter, with order 5 (wavelengths: [8670–8750 Å]) having the lowest $\sigma_{T_{\text{eff}}}$ value and order 17 (wavelengths: [10460–10570 Å]) having the lowest $\sigma_{\text{Fe}/\text{H}}$ value. In addition, Table 1 shows the individual best-fit stellar parameter point estimates for G 9-40 for the same orders. The derivation of the point estimates is further discussed in Section 3.1.4.

Although all of the orders considered perform similarly in the cross-validation, we elect to use order 17 for our stellar parameter point estimate, as that order has the highest S/N and this order has some of the fewest telluric absorption lines of the orders considered, minimizing systematic errors from telluric absorption. Further, this order empirically shows a slightly better performance in recovering the known metallicity. Although we do not observe G 9-40 to exhibit significant chromospheric Ca infrared (IRT) activity from inspection of the HPF spectra, we elect not to use order 5 for our final spectral parameter point estimate (although it formally shows the lowest $\sigma_{T_{\text{eff}}}$ value in our cross-validation), as that order contains one of the Ca IRT lines that can be in emission for active stars and could adversely affect the χ^2 comparison. As such, using the cross-validation results for order 17, we assign $\sigma_{T_{\text{eff}}} = 73 \text{ K}$,

Table 1

Results of Stellar Parameter Estimation for G 9-40 for the HPF Orders Considered (see Section 3.1.4), with the Library Cross-validation Residual Standard Deviations (see Section 3.1.3) for the Same Orders

Order	Wavelength Region (Å)	S/N	G 9-40 Best-fit Values			Library Cross-validation		
			T_{eff} (K)	Fe/H (dex)	log g (dex)	$\sigma_{T_{\text{eff}}}$ (K)	$\sigma_{\text{Fe/H}}$ (dex)	$\sigma_{\log g}$ (dex)
5	[8670, 8750]	85	3426	-0.084	4.896	64	0.15	0.05
6	[8790, 8885]	90	3420	-0.031	4.860	83	0.18	0.06
14	[9940, 10055]	126	3366	-0.048	4.878	100	0.17	0.06
15	[10105, 10220]	131	3378	-0.063	4.873	86	0.17	0.05
16	[10280, 10395]	134	3381	-0.061	4.898	69	0.15	0.05
17	[10460, 10570]	138	3405	-0.078	4.909	73	0.13	0.05

Notes. The cross-validation standard deviations are the standard deviation of the residuals between the recovered and known library values of all of the stars in the stellar library. We assign the cross-validation standard deviations as our error on the corresponding stellar-parameter estimate. For the spectroscopic stellar-parameter point estimates, we see that all of the orders yield consistent parameters within the error bars determined from the library cross-validation. We adapt the boldface values as the stellar parameters of G 9-40. Figure 3 graphically depicts the individual library residuals for order 17, our highest S/N order, and we assign the stellar parameters derived from order 17 as our final parameters for G 9-40, as is further discussed in Section 3.1.3.

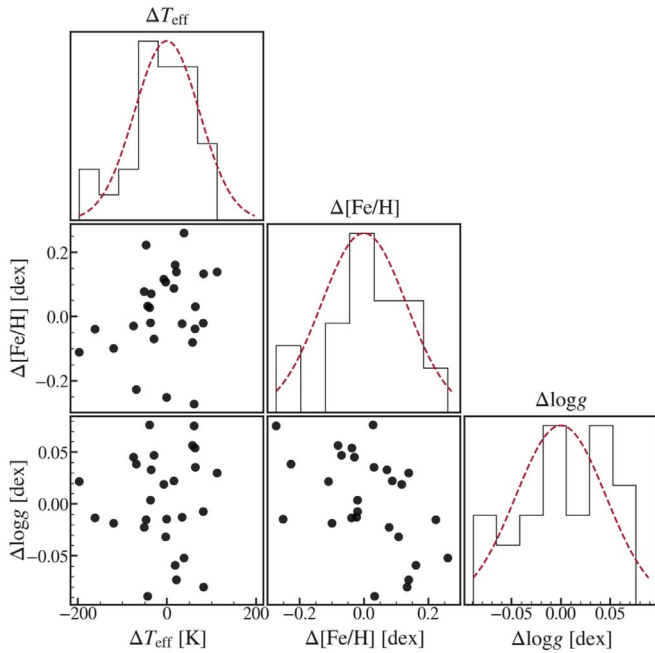


Figure 3. Cross-validation of the empirical spectral-matching algorithm using a leave-one-out approach for HPF order 17, showing the difference (denoted by Δ) between the recovered stellar-parameter value and the known value for each star in the library for T_{eff} , [Fe/H], and log g . The standard deviations of the three parameters are 73 K, 0.13 dex, and 0.05 dex for T_{eff} , Fe/H, and log(g), respectively. We obtain a similar level of scatter using the other HPF orders, as summarized in Table 1. The dotted red line compares the corresponding histograms to the expected Gaussian distribution centered around zero with the same standard deviation as the observed data.

$\sigma_{\text{Fe/H}} = 0.13$ dex, and $\sigma_{\log g} = 0.05$ dex as our best estimates of the 1σ errors for our point estimates of T_{eff} , [Fe/H], and log g , respectively. Figure 3 graphically shows the cross-validation residuals for order 17.

3.1.4. G 9-40 Parameter Estimation

We ran the spectral-matching algorithm described above on the highest-S/N spectrum of G 9-40, which had an S/N of 148 at $\sim 1.1 \mu\text{m}$ and an S/N of 137 in order 17. The top panels in Figure 4 visualize the χ^2_{initial} values as calculated using

Equation (1) for all of the library stars in the T_{eff} and [Fe/H] plane (left) and the T_{eff} and log g plane (right). The five best-matching stars (GJ 251, GJ 581, GJ 109, GJ 1148, and GJ 105 B) are highlighted in red in the upper panels in Figure 4. We then used these five best-matching stars for the second linear combination step optimizing the $\chi^2_{\text{composite}}$ value in Equation (2). The lower panel in Figure 4 compares the spectra of these five stars, along with the best-fit linearly combined composite spectrum. The final composite spectrum and the corresponding residuals from the target star are shown at the bottom. Using the weights, we determine the following stellar parameters for G 9-40 using order 17: $T_{\text{eff}} = 3405 \pm 73$ K, $\text{Fe/H} = -0.078 \pm 0.13$, and $\log(g) = 4.909 \pm 0.05$, where our best estimate of the error bars is derived from our cross-validation step for order 17 in Table 1. We note that running the algorithm independently on the other orders in Table 1 results in consistent stellar parameter estimates within the 1σ uncertainties.

3.1.5. Future Work

Although Table 1 demonstrates that the current version of our spectral-matching framework with HPF spectra is performing reliably, we discuss a number of future work topics here that could further improve its performance. This includes correcting the spectra for tellurics using dedicated telluric-removal software, which could unlock the use of other HPF orders for spectral parameter inference. Further, more thorough performance testing is needed at low S/N levels. We have explicitly left this as future work, as all of the spectra in the current library and the spectrum of G 9-40 were all of high S/N (library spectra are all higher than $\text{S/N} > 162$, and the G 9-40 spectrum used has an $\text{S/N} = 148$). Additionally, the algorithm can only infer parameters that are within the bounds of the stellar library. As such, we plan to extend the library to cooler M dwarfs to enable robust spectral parameter estimation of late-type M dwarfs using HPF spectra. Finally, as further noted above, the observed spectral residuals are completely dominated by astrophysical systematics. In the future, we plan to investigate the possibility of adapting the Starfish code (Czekala et al. 2015) to the spectral-matching framework discussed here. Starfish implements a flexible Gaussian process interpolator capable of deriving spectral parameters and posteriors from observed spectra given a spectral library while

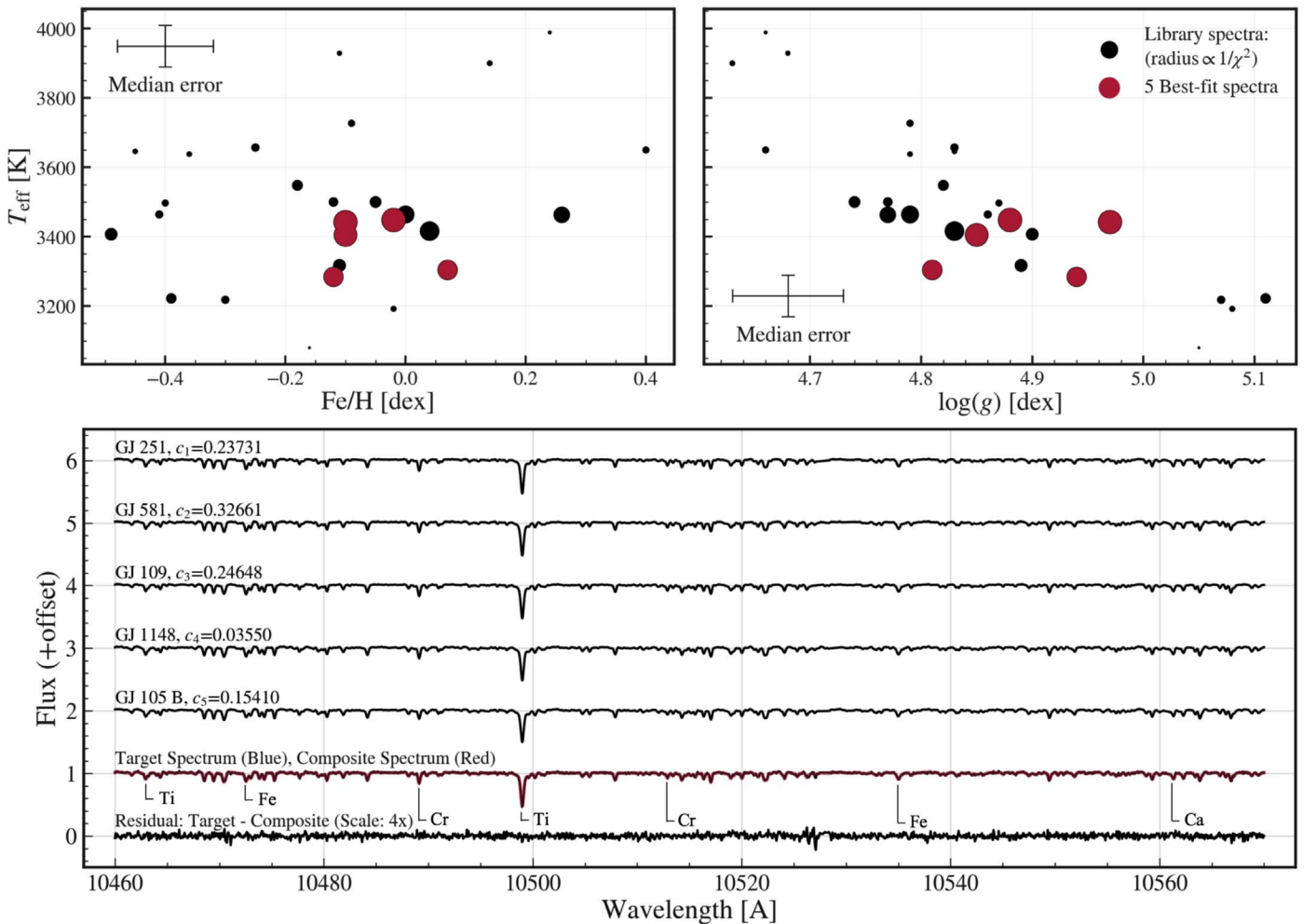


Figure 4. Top panels: best-fit library stars to G 9-40 showing the T_{eff} of the library stars as a function of $[\text{Fe}/\text{H}]$ (left) and $\log g$ (right). The radius of each data point is inversely proportional to the calculated χ^2_{initial} value from Equation (1), so larger points show a lower χ^2_{initial} value and thus indicate a better fit. Highlighted in red are the five best-matching stars: GJ 251, GJ 581, GJ 109, GJ 1148, and GJ 105 B. We use the spectra of these stars to perform a second linear-combination optimization step to interpolate between the stellar parameters of these stars. Bottom: comparison of the five top best-fitting library spectra, the best-fit linear combination spectrum of these five spectra, and the resulting residuals (target G 9-40 spectrum subtracted from the composite spectrum, scaled by a factor of 4). The optimal weights for each of the five library spectra are listed. A few of the atomic lines (Ti, Fe, Cr, Ca) are annotated at the bottom as retrieved from the VALD database (Ryabchikova et al. 2015). Wavelengths are in vacuum wavelengths.

self-consistently accounting for correlated errors in the interpolation between library spectra.

3.2. Spectral Energy Distribution and Isochrone Fitting

To estimate the mass, radius, and age of G 9-40, we use EXOFASTv2 to perform a spectral energy distribution (SED) and isochrone fit to the available literature photometry (see Table 2), using the *Gaia* parallax and the spectroscopically determined stellar parameters discussed in the previous subsection as Gaussian priors. EXOFASTv2 uses the BT-NextGen Model grid of theoretical spectra (Allard et al. 2012) and the Mesa Isochrones and Stellar Tracks (MIST; Choi et al. 2016; Dotter 2016) to fit the SED and derive model-dependent stellar parameters. To test the consistency of our spectroscopic $\log g$ measurement from our spectral-matching algorithm, we use the same $\log g = 4.909$ value as a starting point for our SED analysis but do not impose a strict prior, to minimize biases on the inferred evolutionary state, mass, and radius of the star (see, e.g., Torres et al. 2012). Figure 5 shows the resulting SED fit. The derived model-dependent stellar

parameters show good agreement with the spectroscopic values derived from the HPF spectra from the previous subsection.

Dressing et al. (2019) provide spectroscopic and photometric estimates of the stellar parameters of G 9-40 that are independent of the parameters presented here. Their spectroscopic estimates are $T_{\text{eff}} = 3264^{+137}_{-121}$ K, $R_* = 0.328^{+0.064}_{-0.054}$ R_{\odot} , $M_* = 0.169^{+0.142}_{-0.153}$ M_{\odot} , and $[\text{Fe}/\text{H}] = -0.202 \pm 0.084$. Their photometric parameters are $T_{\text{eff}} = 3310 \pm 57$ K, $R_* = 0.313 \pm 0.009$ R_{\odot} , and $M_* = 0.295 \pm 0.007$ M_{\odot} , where they adapt the photometric parameters as the best estimate of the stellar parameters. Their adapted parameters are in good agreement with both our spectroscopic stellar parameters and our EXOFASTv2 model-dependent parameters as summarized in Table 2.

3.3. $v \sin i$ and Absolute RV

We measure the projected rotation velocity $v \sin i$ of the star using the high-resolution spectra from HPF, following the method in Reiners et al. (2012). This method compares the CCF of the target spectrum to the resulting CCFs of artificially

Table 2
Summary of Stellar Parameters

Parameter	Description	Value	References
Main Identifiers:			
EPIC	...	212048748	Huber
LSPM	...	J0858+2104	Lepine
2MASS	...	J08585232+2104344	Huber
<i>Gaia</i> DR2	...	684992690384102528	<i>Gaia</i>
Equatorial Coordinates, Proper Motion, and Spectral Type:			
α_{J2000}	Right ascension (R.A.)	08:58:52.32	<i>Gaia</i>
δ_{J2000}	Declination (decl.)	+21:04:34.20	<i>Gaia</i>
μ_{α}	Proper motion (R. A., mas yr ⁻¹)	175.512 ± 0.103	<i>Gaia</i>
μ_{δ}	Proper motion (decl., mas yr ⁻¹)	-318.469 ± 0.067	<i>Gaia</i>
Spectral type	...	M2.5	Reid
Optical and Near-infrared Magnitudes:			
<i>B</i>	APASS Johnson <i>B</i> mag	15.462 ± 0.074	APASS
<i>V</i>	APASS Johnson <i>V</i> mag	13.823 ± 0.040	APASS
<i>g'</i>	APASS Sloan <i>g'</i> mag	14.626 ± 0.047	APASS
<i>r'</i>	APASS Sloan <i>r'</i> mag	13.217 ± 0.061	APASS
<i>i'</i>	APASS Sloan <i>i'</i> mag	11.994 ± 0.061	APASS
<i>Kepler</i> -mag	<i>Kepler</i> magnitude	12.771	Huber
<i>J</i>	2MASS <i>J</i> mag	10.058 ± 0.022	2MASS
<i>H</i>	2MASS <i>H</i> mag	9.433 ± 0.023	2MASS
<i>K_S</i>	2MASS <i>K_S</i> mag	9.190 ± 0.018	2MASS
<i>WISE1</i>	<i>WISE1</i> mag	9.032 ± 0.023	<i>WISE</i>
<i>WISE2</i>	<i>WISE2</i> mag	8.885 ± 0.020	<i>WISE</i>
<i>WISE3</i>	<i>WISE3</i> mag	8.774 ± 0.029	<i>WISE</i>
<i>WISE4</i>	<i>WISE4</i> mag	8.597 ± 0.411	<i>WISE</i>
Spectroscopic Parameters^a:			
T_{eff}	Effective temperature in K	3405 ± 73	This work
[Fe/H]	Metallicity in dex	-0.078 ± 0.13	This work
log(<i>g</i>)	Surface gravity in cgs units	4.909 ± 0.05	This work
Model-dependent Stellar SED and Isochrone Fit Parameters^b:			
T_{eff}	Effective temperature in K	3348 ± 32	This work
[Fe/H]	Metallicity in dex	0.04 ^{+0.10} _{-0.11}	This work
log(<i>g</i>)	Surface gravity in cgs units	4.926 ± 0.027	This work
M_*	Mass in M_{\odot}	0.290 ± 0.020	This work
R_*	Radius in R_{\odot}	0.3073 ^{+0.0059} _{-0.0061}	This work
ρ_*	Density in g cm ⁻³	14.11 ^{+0.99} _{-0.92}	This work
Age	Age in Gyr	9.9 ^{+2.6} _{-4.1}	This work
L_*	Luminosity in L_{\odot}	0.01069 ^{+0.00028} _{-0.00029}	This work
A_v	Visual extinction in mag	0.077 ^{+0.034} _{-0.046}	This work
<i>d</i>	Distance in pc	27.928 ± 0.045	<i>Gaia</i>
π	Parallax in mas	35.807 ± 0.059	<i>Gaia</i>
Other Stellar Parameters:			
P_{rot}	Rotational period in days	29.85 ^{+1.01} _{-0.94}	This work
$v \sin i_*$	Stellar rotational velocity in km s ⁻¹	<2	This work
RV	Absolute radial velocity in km s ⁻¹ (γ)	14.65 ± 0.26	This work

Notes.

^a Derived using our empirical spectral-matching algorithm.

^b EXOFASTv2-derived values using MIST isochrones with the *Gaia* parallax and spectroscopic parameters in *a*) as priors.

References: Huber (Huber et al. 2016), Lepine (Lépine & Shara 2005), Reid (Reid et al. 2004), *Gaia* (Gaia Collaboration 2018), APASS (Henden et al. 2015), UCAC2 (Zacharias et al. 2004), 2MASS (Cutri et al. 2003), *WISE* (Cutri et al. 2014).

broadened spectra of a slowly rotating template star. To calculate the CCF, we use the CCF routines from the publicly available Collection of Elemental Routines for Echelle Spectra

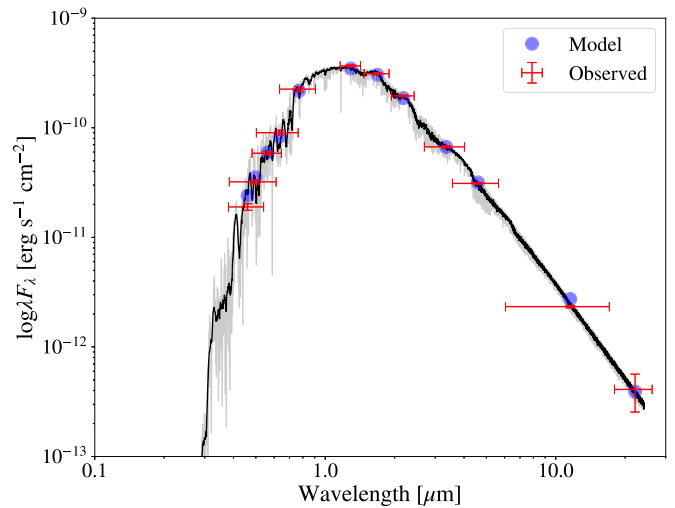


Figure 5. Spectral energy distribution model of G 9-40. The gray line is the raw BT-NextGen model, and the black line is the model smoothed with a boxcar average of 10 points. The SED was fit with EXOFASTv2 using the distance inferred from *Gaia*. The error bars in wavelength reflect the bandwidth of the respective photometric filter, and the error bars in flux reflect the measurement uncertainty. The blue circles are the points on the best-fitting model corresponding to the midpoint of each photometric filter. The resulting stellar parameters are summarized in Table 2.

code base (Brahm et al. 2017), which calculate the CCF by cross-correlating a given spectrum to a fixed binary mask. We elected to use Barnard’s Star as the template star as it is known to be a slow rotator (see, e.g., Ribas et al. 2018) and has a similar spectral type of M4 to G 9-40 of M2.5. To generate the binary mask for the CCF, we used a peak-finding algorithm to find single unblended lines in the Barnard’s Star spectra. Blended lines have been shown to introduce substantial systematic errors in the determination of the $v \sin i$ for relatively small differences in the spectral characteristics of input stars (Reiners et al. 2018). To minimize the impact of tellurics, we only run the peak-finding algorithm on the eight HPF orders cleanest of tellurics (the same eight orders as in the RV analysis in this work). Although relatively clean of tellurics, we further filtered the resulting list to produce a list of lines with minimal telluric overlap using the same telluric mask used for the RV analysis in this work (see Section 2.2). To estimate the scatter in our determination of the $v \sin i$ value, we independently estimated the $v \sin i$ for each of the eight orders separately, resulting in eight independent point estimates of the $v \sin i$. In doing so, all independent orders resulted in a $v \sin i$ at the lower limit of our $v \sin i$ measurement precision (i.e., the width of the target star CCF was fully consistent with the width of the slow-rotator calibrator CCF), suggesting that the $v \sin i$ is below the resolution of HPF. At the resolution of HPF ($R = 55,000$, $\text{FWHM} = 6 \text{ km s}^{-1}$), we estimate that we can detect rotation velocities of about 2 km s^{-1} or more. We thus conclude that G 9-40 has a $v \sin i < 2 \text{ km s}^{-1}$ from the resolution of HPF. This agrees with the slow rotational velocity observed in the *K2* data, as is further discussed in the following subsection.

To measure the absolute RV of G 9-40, we fit a Gaussian profile to the CCF discussed above. Analogous to the $v \sin i$ determination, we fitted each order independently, yielding eight point estimates of the absolute RV. All eight point estimates yielded a consistent value, and we used the standard deviation of the eight different point estimates as our estimate

of the error. This resulted in an absolute RV of $RV = 14.65 \pm 0.26 \text{ km s}^{-1}$, which is also summarized in Table 2.

3.4. Rotation Period

We use the *K2* photometry to estimate the rotation period of G 9-40. Looking at the photometry from *K2* (Figure 7(a)), we see that there are small-scale ($<1\%$) modulations with a period between 25 and 35 days seen on top of a long-term trend after a sharp flux decrease after the first three days. We argue that both the initial sharp flux decrease and the long-term trend are likely not astrophysical (e.g., due to potential systematics including thermal settling of the spacecraft). Therefore, to estimate the rotation period, we remove the first three days and then remove a simple linear trend from the resulting photometry, yielding the light curve shown in Figure 7(b). We then fit the rotation period using two methods as described below.

First, we use the first peak of the autocorrelation function (ACF) as an estimate of the rotation period (see, e.g., McQuillan et al. 2013). To generate the ACF, we used the `acf` function in the `statsmodels` Python package. Before calculating the ACF, we masked the data points during transit, removed any $>3\sigma$ outliers, and then interpolated the masked values to give a uniformly sampled light curve at the ~ 30 minute cadence of *K2*. Figure 6 shows the resulting ACF for the linear-trend-removed photometry in Figure 7(b) along with the location of the highest peak, yielding a rotation period of 27.5 days.

Second, we derived an additional estimate for the rotation period by using a Gaussian process. Angus et al. (2018) show that a quasi-periodic covariance function is effective for making probabilistic measurements of the rotation period even if the data is sparsely sampled. Exact Gaussian process modeling has the disadvantage of the run time scaling as $\mathcal{O}(N^3)$. For this purpose, we use the `juliet` analysis package (Espinoza et al. 2019), which models the photometry using the formalism presented in Foreman-Mackey et al. (2017), where a simple function is constructed that mimics the properties of the quasi-periodic covariance function and implemented with the `celerite` Python package. The period is the only hyperparameter, and there are three nuisance parameters. Using the same data that generated the ACF, we calculate a rotation period of $29.85^{+1.01}_{-0.94}$ days, which is in broad agreement with our rotational period estimate from the ACF method (within 3σ). This results in a maximum stellar equatorial rotational velocity of $v_{\text{eq}} \sim 500 \text{ m s}^{-1}$, in good agreement with the $v \sin i$ constraint in the previous subsection. From the *K2* photometry, the amplitude of the modulation is $\sim 0.5\%$, which could be measured through extensive long-baseline ground-based photometric observations and used to confirm the P_{rot} value presented here. Although they do not present a rotation period estimate, Pepper et al. (2008) classify G 9-40 as a long-period variable using photometric data from the Kilodegree ELT, which is consistent with the rotation period estimate presented here.

4. Transit Analysis

4.1. Transit Search in the *K2* Data

Although Yu et al. (2018) provide an ephemeris for the transits in the *K2* data for EPIC 212048748, we describe our independent transit search here. To search for transits, we flattened the *K2* light curve of G 9-40 using the best-fit GP

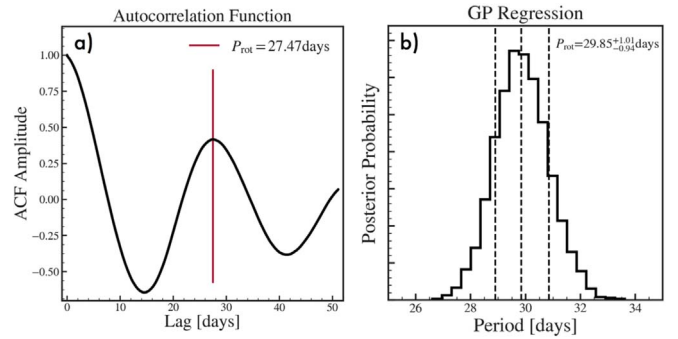


Figure 6. (a) Autocorrelation function of the *K2* photometry after removing transits and removing a linear trend (photometry shown in Figure 7(b)). The red line shows the location of the first peak, suggesting a rotation period of $P_{\text{rot,acf}} = 27.47$ days. (b) Rotational period posteriors from our quasi-periodic kernel Gaussian process (GP) regression of the same photometry as in (a), suggesting a rotational period of $P_{\text{rot,gp}} = 29.85^{+1.01}_{-0.94}$ days.

model from *Everest*. We then ran a Fortran and Python implementation²⁸ of the box least squares (BLS) algorithm (Kovács et al. 2002) on the flattened light curve. After finding a significant periodic signal using the BLS algorithm, we masked $2 \times T_{14}$ transit-time windows surrounding the calculated transit midpoints and then reran the BLS algorithm to look for potential further transits. We found no strong evidence for other transits in the system. The final *K2* photometry from *Everest* is shown in Figure 7 along with the identified transits.

4.2. Transit Fitting

After identifying the transit locations using the BLS algorithm, we ran three different fits: a fit of the *K2* transits only, a fit of the ground-based transit only, and finally a joint fit with the *K2* and ground-based transits simultaneously to put further constraints on the orbital period. We performed all transit fits in a Markov Chain Monte Carlo (MCMC) framework to obtain parameter posteriors following the methodology described in Stefansson et al. (2017, 2018a). In short, for all three fits, we used the `batman` Python package for the transit model, which uses the transit model formalism from Mandel & Agol (2002). Before starting the MCMC runs, we found the global best-fit solution using a differential-evolution global optimization package called `PyDE`,²⁹ maximizing the log-posterior probability (sum of the log-likelihood function and log prior probabilities). We initialized 100 walkers distributed in a uniform N -dimensional sphere (where N is the number of jump parameters used) close to the maximum-likelihood solution using the `emcee` affine-invariant MCMC ensemble sampler (Foreman-Mackey et al. 2013). We computed 50,000 steps for each Markov Chain walker, resulting in a total of 5,000,000 computed samples. We removed the first 5000 steps in each chain as burn-in, resulting in 4,500,000 samples used for final parameter inference. The Gelman–Rubin statistics for the resulting chains were all $<3\%$ from unity, which we considered well mixed (see, e.g., Ford 2006).

We used the following five MCMC jump parameters describing the planet transit: transit center (T_C), period ($\log(P)$), inclination ($\cos(i)$), radius ratio (R_p/R_*), and semimajor axis ($\log(a/R_*)$),

²⁸ The BLS package is openly available on GitHub: <https://github.com/dfm/python-bls>.

²⁹ <https://github.com/hpparvi/PyDE>

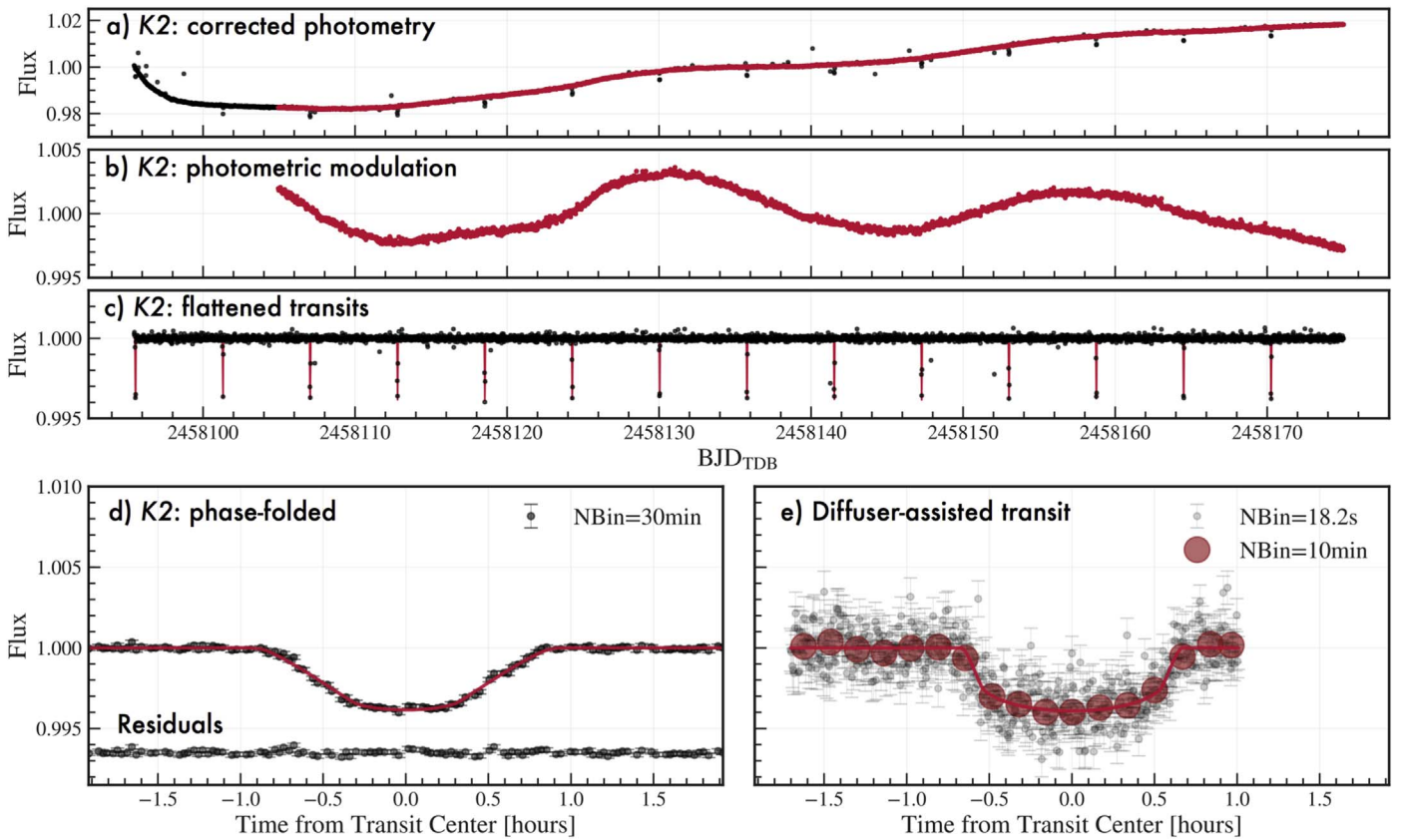


Figure 7. *K2* and ground-based diffuser-assisted photometry of G 9-40. (a) *K2* photometry from the *Everest* pipeline in black after correcting the *K2* data for pointing drifts and thruster events. Transits are clearly seen. The red curve is used to estimate the photometric rotation period of G 9-40 after removing a linear trend (see panel (b)) and any transits. (b) Subset of the full *K2* photometry used to estimate the photometric rotation period after removing a linear trend and the first 400 points from panel (a). Further, any transits have been masked out and linearly interpolated over to generate a homogeneously sampled curve to calculate an ACF to estimate the rotation period (see Figure 6). (c) Flattened light curve in black (same as black curve in (a)) after flattening with our best-fit GP model from *Everest*. Our best-fit transit model is shown in red. (d) Phase-folded *K2* photometry along with the best-fit model in red. (e) Ground-based diffuser-assisted photometry in the custom Semrock 857/37 nm filter using the ARCTIC imager on the 3.5 m ARC Telescope at APO. Black points have a cadence of 18.2 s, and the red points show the photometry binned to a 10 minute cadence.

(The data used to create this figure are available.)

along with one parameter for the out-of-transit baseline flux. We explicitly fix the eccentricity and the argument of periastron to be equal to zero. We impose broad uniform priors on all five jump parameters that are summarized in Table 3. For T_C , $\log(P)$, and R_p/R_* , we center the priors on the values determined by the BLS algorithm, but as we do not get constraints on the values of $\log(a/R_*)$ and $\cos(i)$ from the BLS algorithm, we imposed wide uniform priors on these parameters. We impose a Gaussian prior centered on unity for the baseline flux parameter. We used a quadratic limb-darkening law to describe the limb-darkening using the triangular-sampling parameterization described in Kipping (2013). Following Kipping (2013), we fully marginalize over the complete parameter space of the q_1 and q_2 limb-darkening coefficients (from 0 to 1) to minimize biases on our planet parameter values due to inaccuracies in the stellar parameters.

Table 3 summarizes the priors used for all of the different fits. We report the median values along with the 16th and 84th percentile error bars derived from the posteriors for all three fits in Table 4. Our joint-fit median values collectively provide a good description of the transit (i.e., no obvious bimodality is seen in the resulting posteriors). We further note that our resulting best-fit transit parameters are consistent within the 1σ error bars with the parameters obtained by Yu et al. (2018). We

further compare our resulting transit ephemeris to the ephemeris obtained by Yu et al. (2018) in Section 6.

4.2.1. *K2* Light Curve Analysis

To reduce the data volume of the *K2* data to be analyzed, we clipped the light curve in $2 \times T_{14}$ windows—where T_{14} is the transit duration between first and fourth contact—surrounding the expected transit midpoints (after flattening the light curve and removing any 4σ outliers) using the best-fit *Everest* GP detrending model. Using the `exposure_time` keyword in the `batman` package, we oversampled and binned the model to reflect the 30 minute *Kepler* cadence as suggested by Kipping (2010). For the transit modeling, we fixed the error bar per photometric observation to the standard deviation of all of the points outside the transit but within the $2 \times T_{14}$ transit window, resulting in a fixed error estimate of $\sigma_{30 \text{ min}, K2} = 130$ ppm. In addition to this, in our MCMC fits, we also experimented fitting for the optimal *K2* error bar by including the error bar as a free parameter in the *K2* fit, which resulted in a consistent error estimate. As both values agreed, we elected to keep the *K2* error bar estimate fixed, to reduce the number of free parameters in the fit. The MCMC jump parameters and associated priors for this fit are summarized in Table 3.

Table 3
Summary of Priors Used for the Three MCMC Transit Fits Performed

Parameter	Description	<i>K2</i> -only	Ground-only	Joint
$\log(P)$ (days)	Orbital period	$\mathcal{U}(0.7592, 0.7594)$	$\mathcal{N}(0.75936, 0.00002)$	$\mathcal{U}(0.7592, 0.7594)$
T_C	Transit midpoint (BJD _{TDB})	$\mathcal{U}(2458095.54, 2458095.56)$	$\mathcal{U}(2458497.76, 2458497.80)$	$\mathcal{U}(2458497.76, 2458497.80)$
$(R_p/R_*)_{K2}$	Radius ratio	$\mathcal{U}(0, 0.1)$...	$\mathcal{U}(0, 0.1)$
$(R_p/R_*)_{\text{ground}}$	Radius ratio	...	$\mathcal{U}(0, 0.1)$	$\mathcal{U}(0, 0.1)$
$\cos(i)$	Transit inclination	$\mathcal{U}(0, 0.2)$	$\mathcal{U}(0, 0.2)$	$\mathcal{U}(0, 0.2)$
$\log(a/R_*)$	Normalized orbital radius	$\mathcal{U}(0.9, 2.0)$	$\mathcal{U}(0.9, 2.0)$	$\mathcal{U}(0.9, 2.0)$
fraw_{K2}	Transit baseline for <i>K2</i> data	$\mathcal{U}(0.9, 1.1)$...	$\mathcal{N}(1.00002, 0.0002)$
$\text{fraw}_{\text{Ground}}$	Transit baseline for ground-based data	...	$\mathcal{U}(0.9, 1.1)$	$\mathcal{N}(1.001, 0.001)$
D_{Line}	Ground detrend parameter: line	...	$\mathcal{U}(-0.1, 0.1)$	$\mathcal{N}(0.00104, 0.00001)$

Notes. $\mathcal{N}(m, \sigma)$ denotes a normal prior with mean m and standard deviation σ ; $\mathcal{U}(a, b)$ denotes a uniform prior with a start value a and end value b . The eccentricity was assumed to be zero for all fits. For all fits, we uniformly sampled quadratic limb-darkening parameters q_1 and q_2 from 0 to 1 using the formalism from Kipping (2013). Priors on T_{eff} and R_* are adapted from Table 2, but no prior is placed on the stellar density ρ .

Table 4
Median Values and 68% Confidence Intervals for the Transit Fit Parameters for Our *K2*-only, Ground-based-only, and Joint *K2* and Ground-based MCMC Analyses

Parameter	Description	<i>K2</i>	Ground	Joint Fit (Adopted)
$T_C(\text{BJD}_{\text{TDB}})$	Transit midpoint	$2458095.55737^{+0.00030}_{-0.00030}$	$2458497.77751^{+0.00036}_{-0.00036}$	$2458497.77747^{+0.00032}_{-0.00033}$
P (days)	Orbital period	$5.745951^{+0.00004}_{-0.00004}$	$5.74596^{+0.00026}_{-0.00026}$	$5.746007^{+0.00006}_{-0.00006}$
$(R_p/R_*)_{K2}$	Radius ratio (<i>K2</i>)	$0.059^{+0.0035}_{-0.0026}$...	$0.0605^{+0.0026}_{-0.0028}$
$(R_p/R_*)_{\text{ground}}$	Radius ratio (ground)	...	$0.0635^{+0.0031}_{-0.0047}$	$0.0605^{+0.0032}_{-0.0033}$
$R_{p,K2}(R_{\oplus})$	Planet radius (<i>K2</i>)	$1.981^{+0.12}_{-0.095}$...	$2.025^{+0.096}_{-0.097}$
$R_{p,\text{ground}}(R_{\oplus})$	Planet radius (ground)	...	$2.13^{+0.12}_{-0.16}$	$2.03^{+0.11}_{-0.11}$
$\delta_{p,K2}$	Transit depth (<i>K2</i>)	$0.00348^{+0.00043}_{-0.00030}$...	$0.00365^{+0.00032}_{-0.00033}$
$\delta_{p,\text{ground}}$	Transit depth (ground)	...	$0.00403^{+0.00041}_{-0.00058}$	$0.00366^{+0.00039}_{-0.00039}$
a/R_*	Normalized orbital radius	$29.8^{+5.8}_{-7.6}$	$22.4^{+6.4}_{-2.9}$	$27.0^{+5.4}_{-3.7}$
a (au)	Semimajor axis (from a/R_* and R_*)	$0.0425^{+0.0082}_{-0.011}$	$0.032^{+0.0092}_{-0.0042}$	$0.0385^{+0.0078}_{-0.0053}$
$\rho_{*,\text{transit}}$ (g cm^{-3})	Density of star	$15.1^{+11.0}_{-8.9}$	$6.4^{+7.2}_{-2.2}$	$11.2^{+8.3}_{-4.0}$
i ($^\circ$)	Transit inclination	$88.88^{+0.79}_{-0.97}$	$87.98^{+0.85}_{-0.49}$	$88.57^{+0.63}_{-0.47}$
b	Impact parameter	$0.58^{+0.23}_{-0.38}$	$0.788^{+0.064}_{-0.20}$	$0.672^{+0.100}_{-0.22}$
e	Eccentricity	0.0 (adopted)	0.0 (adopted)	0.0 (adopted)
ω ($^\circ$)	Argument of periastron	0.0 (adopted)	0.0 (adopted)	0.0 (adopted)
T_{eq} (K)	Equilibrium temp. (assuming $a = 0.3$)	$304.0^{+48.0}_{-26.0}$	$350.0^{+26.0}_{-42.0}$	$319.0^{+25.0}_{-28.0}$
T_{eq} (K)	Equilibrium temp. (assuming $a = 0.0$)	$434.0^{+69.0}_{-37.0}$	$500.0^{+37.0}_{-59.0}$	$456.0^{+35.0}_{-40.0}$
S (S_{\oplus})	Insolation flux	$5.9^{+4.7}_{-1.8}$	$10.4^{+3.4}_{-4.1}$	$7.2^{+2.5}_{-2.2}$
T_{14} (days)	Transit duration	$0.0546^{+0.0026}_{-0.0018}$	$0.0583^{+0.0026}_{-0.0025}$	$0.0557^{+0.0019}_{-0.0017}$
τ (days)	Ingress/egress duration	$0.0044^{+0.0044}_{-0.0015}$	$0.0086^{+0.0035}_{-0.0040}$	$0.0056^{+0.0023}_{-0.0019}$
$T_5(\text{BJD}_{\text{TDB}})$	Time of secondary eclipse	$2458098.43034^{+0.00028}_{-0.00028}$	$2458500.65049^{+0.00039}_{-0.00038}$	$2458500.65047^{+0.00032}_{-0.00033}$

Notes. For our joint fit, we fit for the transit depth (δ) and the planet radius ratio (R_p/R_*) separately for *K2* and the diffuser-assisted observations, resulting in slightly different values derived for the planet radii and transit depths in the two different bands. These values are denoted by (*K2*) and (ground), respectively. We fixed the eccentricity and argument of periastron to zero for all fits.

4.2.2. Ground-based Light Curve Analysis

For the ground-based analysis, we estimate the photometric uncertainty, including scintillation, following the discussion surrounding Equation (3) in Stefansson et al. (2018a), yielding error bars that account for photon, dark, readout, background, digitization, and scintillation noise. For the scintillation error calculation, we assumed that the single reference star used was fully uncorrelated to the scintillation error from the target star. The jump parameters, along with the associated priors for this fit, are summarized in Table 3. In addition to the transit jump parameters, in this MCMC fit we also simultaneously detrend with a line to account for a low-amplitude linear slope observed in the photometry.

In Figure 8, we show the photometric precision (or the rms of the best-fit residuals) as a function of bin size using the MC3 package from Cubillos et al. (2017), which estimates error bars on the rms values assuming they follow an inverse gamma distribution. Additionally, shown in red in Figure 8 is the expected bin-down behavior assuming Gaussian white noise. From Figure 8, we see that in our ground-based observations, we achieve a photometric precision of $\sigma_{\text{unbin}} = 1225$ ppm unbinned (18.2 s cadence), which bins down to $\sigma_{1 \text{ min}} = 689 \pm 37$ ppm and $\sigma_{30 \text{ min}} = 88^{+52}_{-27}$ ppm, in 1 minute and 30 minute bins, respectively. For comparison, we note that the Gaussian expected precision in 30 minutes is 138 ppm. We observe that the rms values largely follow the expected white-noise behavior, although we note that slight excursions below

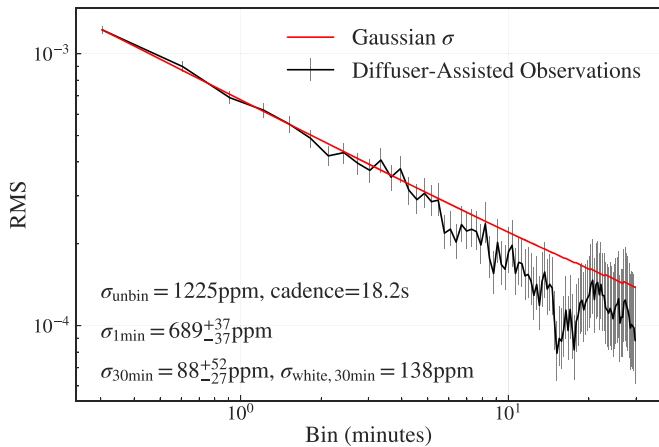


Figure 8. The rms value of the residuals of the ground-based diffuser-assisted photometry as a function of bin size in minutes (black curve) compared to the Gaussian expected bin-down behavior shown in red. We see that the data largely bin down as Gaussian white noise, with some downward excursions below the expected Gaussian behavior seen at the largest bin sizes. We conservatively say that we reach a precision of 138 ppm in 30 minutes.

the Gaussian expected values are observed at the largest bin sizes, which still are largely consistent with the Gaussian expected precision within the reported error bars. Similar and larger departures below the Gaussian expected precision have been reported by a number of groups in the literature (e.g., Blečić et al. 2013; Stefansson et al. 2017), and Cubillos et al. (2017) show that these excursions are not statistically significant after taking into account the increasingly skewed inverse gamma distribution of the rms values at the largest bin sizes. Following our previous work (Stefansson et al. 2017, 2018a), we argue that excursions much below the Gaussian expected precision are likely an overestimate of the actual precision achieved, and we conservatively say that we achieve 138 ppm precision in 30 minute bins for these transit observations.

4.2.3. Joint K2 and Ground-based Light Curve Analysis

To further constrain the planet parameters, in addition to the individual K2 and ground-based-only fits discussed above, we performed a joint fit of both the K2 and the ground-based observations. For this fit, we imposed uniform priors on the period and the transit center, and we assume that the planet follows a strictly periodic orbit with no transit timing variations.³⁰ Following Stefansson et al. (2018a), to account for variations in the transit depth due to a potential planetary atmosphere, we allowed the radius ratio R_p/R_* to vary separately for the K2 and ground-based data, while assuming common values for the $\log(P)$, T_C , $\log a/R_*$, and $\cos(i)$ parameters. We include independent parameters for the transit baselines, and we perform a simultaneous linear detrend for the ground-based observations as discussed in the previous subsection. Similarly, for the K2-only fit, we fix the K2 error bar at 130 ppm for each individual photometric point from K2. The priors we used for this fit are summarized in Table 3. Our best-fit joint models are overlaid in red in Figure 7 in panels (c), (d), and (e).

³⁰ We see no obvious signs of transit timing variations (TTVs) in the phase-folded K2 transits, and the transit center of our diffuser-assisted observations is consistent with our K2-only linear ephemeris (see Section 6.1).

5. Statistical Validation and False-positive Analysis

To estimate the probability that the transits observed by K2 were due to astrophysical false positives, we used the VESPA (Morton 2012, 2015) code. The VESPA algorithm statistically validates a planet by simulating and determining the likelihood of a range of astrophysical false-positive scenarios that could replicate the observed light curve. VESPA generates a population of 20,000 systems for each false-positive scenario, which includes background eclipsing binaries (BEBs), eclipsing binaries (EBs), and hierarchical eclipsing binaries (HEBs), to calculate the likelihoods. As input to VESPA, we used the (1) 2MASS JHK , SDSS $g'r'i'$, and *Kepler* magnitudes; (2) *Gaia* parallax; (3) host star temperature, surface gravity, and metallicity derived from our HPF observations; and (4) the maximum visual extinction from estimates of Galactic dust extinction (Green et al. 2019). These values are summarized in Table 2.

Two additional constraints needed for the VESPA statistical analysis are the maximum separation for a background eclipsing object and the maximum depth of the occultation. We adopted the maximum radius from the EVEREST photometric aperture ($16''$) as the maximum allowed separation between the G 9-40 and the true source of the transit event. To obtain the maximum occultation depth, we followed the procedure used by Dressing et al. (2017). We phase-folded the K2 photometry to the period of G 9-40b and fit a light curve model to the data. The occultation was forced to have the same duration as the transit but was not constrained to be circular such that the center was allowed to float between phases 0.3 and 0.7. We record the depth at various points in this region of the light curve and adopt the maximum value as the maximum occultation depth. We performed the analysis with VESPA on the K2 light curves with the R_p/R_* ratio in the *Kepler* bandpass set to the 16th, 50th, and 84th percentiles of the posterior distribution from this work. The results for various false-positive scenarios considered are shown in Table 5. This analysis yielded a false-positive possibility (FPP) of $FPP < 1 \times 10^{-6}$, which we conclude statistically validates G 9-40b as a planet.

Although not included directly in the VESPA analysis, our HPF radial velocities, which are further discussed in Section 6.4, further bolster the planetary interpretation as no significant RV signal is detected. We use these RVs to provide an upper limit on the mass of G 9-40b, as is further discussed in Section 6.4.

6. Discussion

6.1. Updated Ephemeris

To enable better future scheduling of transit observations, we fit our ground-based diffuser transit and the K2 transits together to provide an updated ephemeris of G 9-40b. Figure 9 compares errors on the transit center as a function of time into the beginning of the JWST era. From our K2-only fit (blue curve), we see that the expected errors are ~ 13 minutes at the start of the JWST era in 2021. However, from our updated joint-fit ephemeris (green curve), we reduce this error by a factor of 8 down to ~ 1.7 minutes. We further see that our ground-based transit was observed at the upper edge of our 1σ error bar estimate from our K2-only fit.

In Figure 9 we additionally compare our ephemerides to the ephemerides presented in Yu et al. (2018) calculated from K2 Campaign 16 data only (purple curve). We see that there is a

Table 5

VESPA FPPs for Various False-positive Scenarios Calculated using the 16th, 50th, and 84th Percentiles of the R_p/R_* Posterior Probability Distribution from Our Joint K2 and Ground-based Transit Fit Described in Section 4

R_p/R_* Percentile	EB FPP	HEB FPP	BEB FPP	Total FPP
16	$(29.8 \pm 5.9) \times 10^{-9}$	$(11.2 \pm 7.6) \times 10^{-8}$	$<1 \times 10^9$	$(14.2 \pm 7.4) \times 10^{-8}$
50	$(27.1 \pm 4.9) \times 10^{-9}$	$(4.3 \pm 2.6) \times 10^{-8}$	$(1.0 \pm 1.4) \times 10^{-8}$	$(8.1 \pm 2.8) \times 10^{-8}$
84	$(36.5 \pm 7.5) \times 10^{-9}$	$(12.7 \pm 6.1) \times 10^{-8}$	$(1.8 \pm 2.0) \times 10^{-8}$	$(18.2 \pm 6.4) \times 10^{-8}$

Note. All other input values are identical in each run. The values reported are the mean and standard deviation of a bootstrap of 10 samples for each individual run.

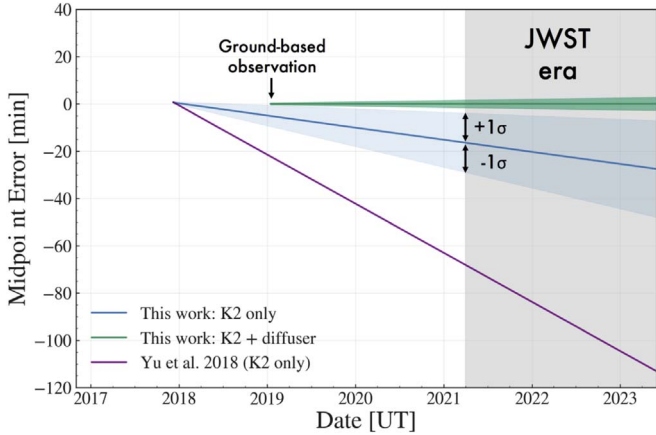


Figure 9. Evolution of the G 9-40b transit ephemeris uncertainties into the JWST era. The blue and green curves show the transit ephemeris derived from our K2-only fit and our joint K2 and diffuser-assisted transit fits, respectively. Additionally shown are the associated 1σ error bands in the shaded areas. We show that our joint K2 and diffuser-assisted fit reduces the expected uncertainty in the ephemerides in the JWST era from ~ 13 minutes down to ~ 1.7 minutes, allowing for efficient scheduling of future characterization observations during transit. Additionally shown is the transit ephemeris from Yu et al. (2018) in purple (no uncertainty estimate is available), which is discrepant to the ephemeris reported here.

discrepancy between the ephemerides derived in this work and the ephemerides presented in Yu et al. (2018). As mentioned above, our ground-based transit was observed at the upper edge of our 1σ error bar estimate from our K2-only fit, whereas our ground-based transit was observed ~ 23 minutes later than expected from the Yu et al. (2018) ephemeris (no uncertainty estimate is reported in Yu et al. 2018 on the ephemeris). We attribute the discrepancy to the different photometric reduction and detrending methods, and we prefer the ephemeris reported here for the planning of future transit observations, given the consistency of the K2-only fits and our ground-based transit observations.

6.2. Stellar Density

We used our joint transit model to get an independent estimate of the stellar density, using the equation from Seager & Mallén-Ornelas (2003),

$$\rho_{*,\text{transit}} = \frac{3\pi}{GP^2} \left(\frac{a}{R_*} \right)^3, \quad (4)$$

where G is the gravitational constant, and the eccentricity is assumed to be zero. From Table 2, we see that our stellar density derived from our stellar radius and mass ($\rho_* = 14.11^{+0.99}_{-0.92} \text{ g cm}^{-3}$) is consistent with the stellar density derived from our transit observations ($\rho_{*,\text{transit}} = 11.2^{+8.3}_{-4.0} \text{ g cm}^{-3}$).

6.3. Predicted Most-likely Mass Estimate

We predict the most-likely mass of G 9-40b using two different methods. First, we use the Forecaster Python package (Chen & Kipping 2017), which adopts a broken-power-law model to model the exoplanet MR relation and is capable of predicting the masses of exoplanets given their radii. Using Forecaster, we obtain an expected mass of $M = 5.04^{+3.79}_{-1.91} M_{\oplus}$, which yields an expected RV semi-amplitude of $K = 4.11^{+3.08}_{-1.56} \text{ m s}^{-1}$ assuming a circular orbit. Figure 10 shows the expected mass and RV-semi-amplitude posteriors as calculated using Forecaster. Further, using these posteriors, Forecaster is capable of classifying the planet as Terrian, Neptunian, Jovian, or stellar. From the posteriors in Figure 10, Forecaster classifies G 9-40b as Neptunian with 99.7% confidence.

Second, we compare our predicted mass from Forecaster to the value from the MRExO toolkit. As is discussed in Kanodia et al. (2019), MRExO offers two different MR relations for forecasting: a Kepler planet-sample MR relation, and an M dwarf-planet MR relation. For this fit, we used the M dwarf-planet MR relation given the M2.5 spectral type of the host star, yielding a predicted mass of $M = 3.94^{+11.5}_{-3.3} M_{\oplus}$. Although both values are within the formal error bars of each other, we note that the median value from MRExO is smaller than the $M = 5.04^{+3.79}_{-1.91} M_{\oplus}$ value we obtain from Forecaster. Further, the MRExO value has a larger spread than the value from Forecaster. This larger spread is noted in Kanodia et al. (2019) as being due to the nonparametric fitting technique and the low number of M dwarf-only planets in the M dwarf-MR relation used by MRExO, resulting in a less-precise estimate.

Assuming a median semi-amplitude of 4 m s^{-1} , this shows that G 9-40b can be followed up with a number of high-precision RV instruments already online or under construction (Fischer et al. 2016; Wright & Robertson 2017). As noted by Kanodia et al. (2019), there are rising statistical trends that suggest a difference between the exoplanet MR relation between M dwarfs and exoplanets orbiting earlier-type stars. However, the comparison of the two populations is still limited by the low number of M dwarf planets with both precise radii and masses. With a measurement of its mass, G 9-40b will yield further direct insights into those statistical trends.

6.4. Upper Bound on Mass Estimate Using the HPF RVs

To further constrain possible false-positive binary scenarios and to provide an upper bound of the mass of G 9-40b, Figure 11(a) shows the RVs of G 9-40 as a function of time as observed by HPF (Table 6 lists the RVs in tabular format). The blue points are individual 945 s exposures ($\sigma_{\text{unbinned}} = 6.49 \text{ m s}^{-1}$), whereas the red points show weighted-average RVs per individual HET track ($\sigma_{\text{binned}} = 5.32 \text{ m s}^{-1}$; effective exposure time of $2 \times 945 \text{ s} = 31.5$ minutes). The associated

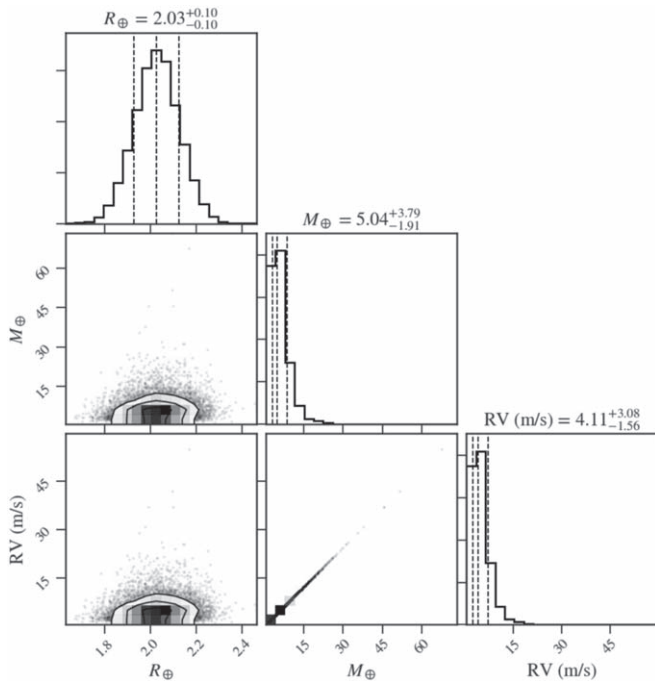


Figure 10. Probabilistic RV semiamplitudes and masses calculated from the measured radii using *Forecaster* (Chen & Kipping 2017). The expected mass and semiamplitude are $M = 5.04^{+3.79}_{-1.91} M_{\oplus}$ and $K = 4.11^{+4.62}_{-2.41} \text{ m s}^{-1}$, respectively. This value agrees well with the mass estimate of $M = 3.94^{+11.5}_{-3.3} M_{\oplus}$ we calculate using the *MRExO* M dwarf exoplanet mass–radius relationship.

error bars as derived from the *SERVAL* pipeline are 9.13 m s^{-1} and 6.23 m s^{-1} for the unbinned and binned points, respectively. Figure 11(b) shows the phase-folded RVs using our best-fit ephemeris from our joint fit in Table 4, showing that our RVs are predominantly located in phases between 0 and 0.4. Further, for comparison, also shown in Figures 11(a) and (b) is the predicted RV curve using our best prediction of the mass of G 9-40b given its radius using the *Forecaster* package ($M = 5.04^{+3.79}_{-1.91} M_{\oplus}$ and $K = 4.11^{+3.08}_{-1.56} \text{ m s}^{-1}$) assuming a circular orbit.

To estimate the upper bound on the mass of G 9-40b, we modeled the RVs in Figure 11 using the *radvel* Python package. For our RV model, we fixed the orbital period and transit center to the joint-fit transit ephemeris in Table 6, and given the small number of RV points, we additionally fixed the orbital eccentricity and argument of periastron to zero. This resulted in a two-parameter RV model using only the orbital semiamplitude (K) and a zero-point offset (γ) as the MCMC jump parameters. For the modeling, we placed minimal uninformative priors on the two parameters, only constraining K to be positive. To sample the parameter space, we initialized 100 MCMC walkers in the vicinity of the expected best-fit solution using the *radvel* MCMC interface. We removed the first marginally well-mixed iterations as burn-in, and we ran the MCMC chains until the Gelman–Rubin statistic was within 0.1% of unity, which we consider indicative of well-mixed chains. Figure 11(c) shows the resulting posteriors of both K and γ . From our fit, we see that the best-fit semi-amplitude for the orbital semi-amplitude is $K = 0.8^{+2.1}_{-0.7} \text{ m s}^{-1}$ (black solid curve in Figures 11(a) and (b)), which is consistent with zero within the $\sim 1\sigma$ lower error estimate. Although the median estimated semi-amplitude from this analysis is lower than our predicted semi-amplitude from both *Forecaster* and *MRExO*

as discussed above, it is within the 2σ error estimates. We attribute the low semi-amplitude we estimate here to a combination of the small number of RV points and their sparse phase coverage of the full RV phase curve, and we argue that more RVs are needed to further test the robustness of this measurement. The semi-amplitude posteriors reported here could be biased by uncorrected astrophysical systematics (e.g., stellar activity), instrumental systematics (e.g., persistence in the HPF H2RG detector; see Metcalf et al. 2019 or Ninan et al. 2019 for a discussion of systematics in NIR RVs from H2RG detectors), or model-mismatch systematics (e.g., an eccentric system, or another unknown planet could be present in the system). With these caveats in mind, we use the resulting posteriors on K to say that, given the current data set and assuming a circular orbit, the semi-amplitude of G 9-40b is $K < 9.0 \text{ m s}^{-1}$ at 99.7% (3σ) confidence. Using our $M = 0.290 \pm 0.020 M_{\odot}$ mass estimate of the host star from Table 2, this translates to an upper limit mass constraint of $M < 11.7 M_{\oplus}$ at 99.7% confidence assuming a circular orbit. If instead we adopt the same priors as discussed above, but let the eccentricity and argument of periastron float (sampled as $\sqrt{e} \cos \omega$ and $\sqrt{e} \sin \omega$ in *radvel*), our best-fit semi-amplitude increases to $K = 21^{+19}_{-12} \text{ m s}^{-1}$, due to the fit favoring a high-eccentricity solution of $e \sim 0.67$ due to the sparse phase sampling of the RVs. Even in the unlikely scenario of such a high-eccentricity orbit, this translates to an upper mass limit of $\sim 0.5 M_J$ at 99.7% confidence, showing that G 9-40 is a planetary-mass object. We prefer the $e = 0$ mass constraint, as we expect G 9-40 to be fully circularized. We estimated a circularization timescale of $\sim 150 \text{ Myr}$ for G 9-40b, following the methodology in Bodenheimer et al. (2001), assuming a tidal quality factor of $Q \sim 10^3$ for a mini-Neptune mass planet (extrapolating between $Q \sim 10^2$ and 10^6 for Earth and Jupiter in the solar system; Goldreich & Soter 1966), which is substantially smaller than our SED estimated age of $9.9^{+2.6}_{-4.1} \text{ Gyr}$, as summarized in Table 2.

6.5. Potential for Future Study

Figure 12 compares G 9-40b to other known planets from the NASA Exoplanet Archive (Akeson et al. 2013) in the exoplanet radius, and exoplanet distance from the solar system plane. At a distance of $d = 27.928 \pm 0.045 \text{ pc}$, G 9-40b is the second-closest transiting planet discovered by *K2* to date, behind the *K2*-129 system from Dressing et al. (2017), which has a *Gaia* DR2 distance of $27.796^{+0.075}_{-0.074} \text{ pc}$.

Being a nearby system, G 9-40 is bright at both visible and NIR wavelengths; for example, G 9-40 is brighter in the *I* band ($I = 10.9$) than GJ 1214 ($I = 11.1$), and only slightly fainter than GJ 1214 ($J = 9.8$) in the *J* band with a *J* magnitude of $J = 10.1$. Due to its relatively large transit depth and the brightness of its host star at NIR wavelengths, G 9-40b is amenable to transmission spectroscopic observations that could provide insight into the planet’s bulk composition and formation history through measuring the elemental composition of its atmosphere and overall metal enrichment. To compare the applicability of performing precision transmission spectroscopic observations of G 9-40 during transit, we calculate the transmission spectroscopy metric (TSM) from Kempton et al. (2018) for G 9-40b and compare it to the corresponding TSM metric for other known exoplanets. Specifically, the TSM metric from Kempton et al. (2018) is

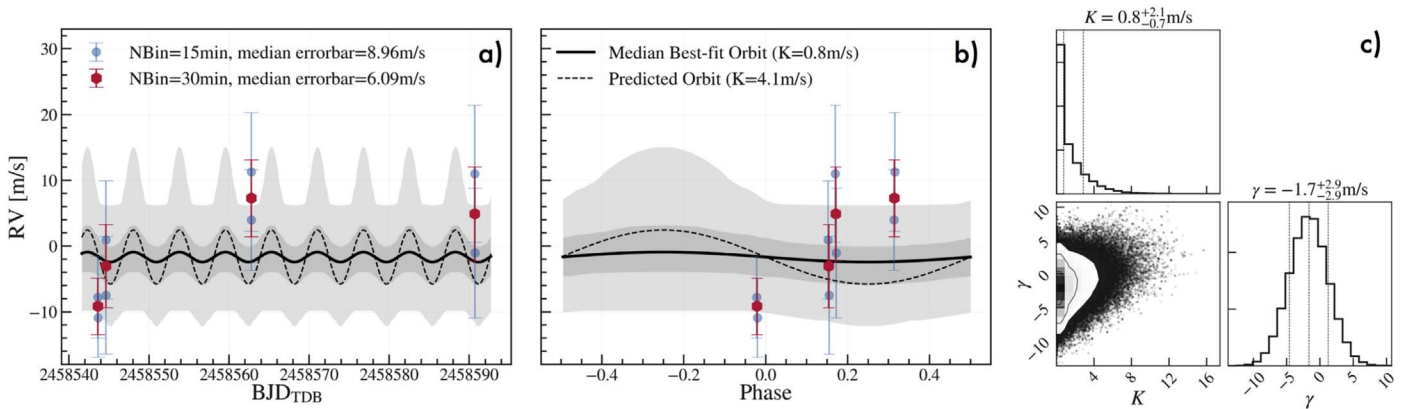


Figure 11. Upper limit on the mass of G 9-40b using RVs from HPF assuming a circular orbit. (a) Radial velocities of G 9-40 from HPF shown as a function of time. Blue points show unbinned RVs (15 minute exposures), and red points show RVs binned per HET track (30 minute exposure equivalent). The solid black curve shows the expected orbit using the ephemeris from Table 4 and using our median predicted mass of $5.04M_{\oplus}$ with a semiamplitude of $K = 4.11 \text{ m s}^{-1}$, estimated using the Forecaster package. The gray shaded regions show the 1σ (dark gray) and 3σ (light gray) envelopes surrounding our median best-fit MCMC model (shown in the solid black curve) of the RVs. (b) Same as in (a), but showing the RVs phased to the best-fit transit ephemeris from Table 4. (c) Posterior correlations between the semiamplitude K and zero-point offset γ from our best-fit MCMC fit to the RVs in (a) and (b). Using the K posteriors from the assumed circular orbit, we conclude that $K < 9.0 \text{ m s}^{-1}$ with 99.7% (3σ) confidence, which corresponds to a mass constraint of $M < 11.7M_{\oplus}$ at 99.7% confidence.

Table 6
Radial Velocities of G 9-40 from HPF

BJD _{TDB}	RV (m s^{-1})	σ_{RV} (m s^{-1})	RV Drift		S/N @1100 nm
			Error (m s^{-1})		
2458543.6173586124	-7.78	6.23	0.02		140.03
2458543.6284200638	-10.90	5.96	0.02		148.49
2458544.622642529	0.94	8.99	0.31		107.54
2458544.6348675573	-7.47	8.94	0.18		106.49
2458562.782749085	3.98	7.65	0.20		131.85
2458562.794474252	11.27	9.04	0.22		113.95
2458590.6907325243	11.00	10.43	0.10		103.96
2458590.7019076305	-1.04	9.85	0.11		108.93

Notes. All exposures are 945 s in length. The derivation of the RV drift error—the contribution of the RV drift of HPF to the total estimated RV error—is described in the Appendix. The total RV error (σ_{RV}) is composed of the error bar given by the SERVAV RV pipeline added in quadrature to our RV drift error estimate.

(This table is available in machine-readable form.)

defined as

$$\text{TSM} = (\text{Scale Factor}) \times \frac{R_p^3 T_{\text{eq}}}{M_p R_*^2} \times 10^{-m_J/5}, \quad (5)$$

where R_p is the radius of the planet in Earth radii, M_p is the mass of the planet in Earth masses, R_* is the radius of the host star in solar radii, T_{eq} is the equilibrium temperature in Kelvin of the planet calculated for zero albedo and full heat redistribution, and m_J is the magnitude of the host star in the J band. Kempton et al. (2018) define the scale factor for different radius bins where

$$\begin{aligned} (\text{Scale Factor}) &= 0.19 & \text{for } R < 1.5R_{\oplus}, \\ (\text{Scale Factor}) &= 1.26 & \text{for } 1.5R_{\oplus} < R < 2.75R_{\oplus}, \\ (\text{Scale Factor}) &= 1.28 & \text{for } 2.75R_{\oplus} < R < 4.0R_{\oplus}. \end{aligned}$$

Further, Kempton et al. (2018) define the TSM metric specifically for *JWST*/NIRISS as NIRISS gives more transmission

spectroscopy information per unit observing time compared to the other *JWST* instruments for a wide range of planets and host stars (Batalha & Line 2017; Howe et al. 2017). For the planets with an unknown mass, we forecast the mass using the prescription suggested in Kempton et al. (2018), using the MR relationship of Forecaster as implemented by Louie et al. (2018).

Using this metric—with G 9-40b falling in the “small sub-Neptune” ($1.5R_{\oplus} < R_p < 2.75R_{\oplus}$) planet size bin—G 9-40b has a high TSM metric of $\text{TSM} = 96^{+64}_{-41}$, assuming a predicted mass of $M = 5.04M_{\oplus}$ using Forecaster, and exceeds the $\text{TSM} > 90$ threshold for high-quality priority atmospheric targets suggested by Kempton et al. (2018). Figure 13 compares the TSM of G 9-40b to the TSM for other currently known planets orbiting M dwarfs ($T_{\text{eff}} < 4000 \text{ K}$ ³¹) with radii less than $4.0R_{\oplus}$ as a function of the host star J magnitude. This plot shows that G 9-40b is currently among the top best small ($< 4.0R_{\oplus}$) M dwarf planets for transmission spectroscopic observations, after GJ 1214b (Charbonneau et al. 2009; $\text{TSM} \sim 615$), the newly discovered mini-Neptune ($R = 1.57R_{\oplus}$) L98-59d orbiting a nearby M3 dwarf (Cloutier et al. 2019; $\text{TSM} \sim 230$), the Neptune-sized ($R = 3.5R_{\oplus}$) M dwarf planet K2-25b in the Hyades (Mann et al. 2016; $\text{TSM} \sim 140$), and the newly discovered sub-Neptune ($R = 2.42R_{\oplus}$) TOI 270c (Günther et al. 2019; $\text{TSM} \sim 130$).

We note that even though G 9-40b has a high TSM metric, the atmosphere of G 9-40b has the possibility of having damped atmospheric features due to its low equilibrium temperature of $T_{\text{eq}} = 319 \text{ K}$ ($a = 0.3$). Past work has shown that hotter planets tend to have larger spectral features, while cooler planets tend to have less prominent features due to hazes (Crossfield & Kreidberg 2017). This has been attributed to the fact that at temperatures below $\sim 1000 \text{ K}$, methane is abundant and can easily photolyze to produce carbon hazes that mute atmospheric features. Even if the atmosphere of G 9-40 is observed to be featureless, as noted by Kempton et al. (2018), the study of a large sample of sub-Neptune exoplanet atmospheres is especially important because these planets do not exist in our solar system, and therefore no well-studied benchmark objects exist. Further,

³¹ The known planet sample was obtained from the NASA Exoplanet Archive with the addition of the newly discovered M3 planetary system L98-59 from Cloutier et al. (2019).

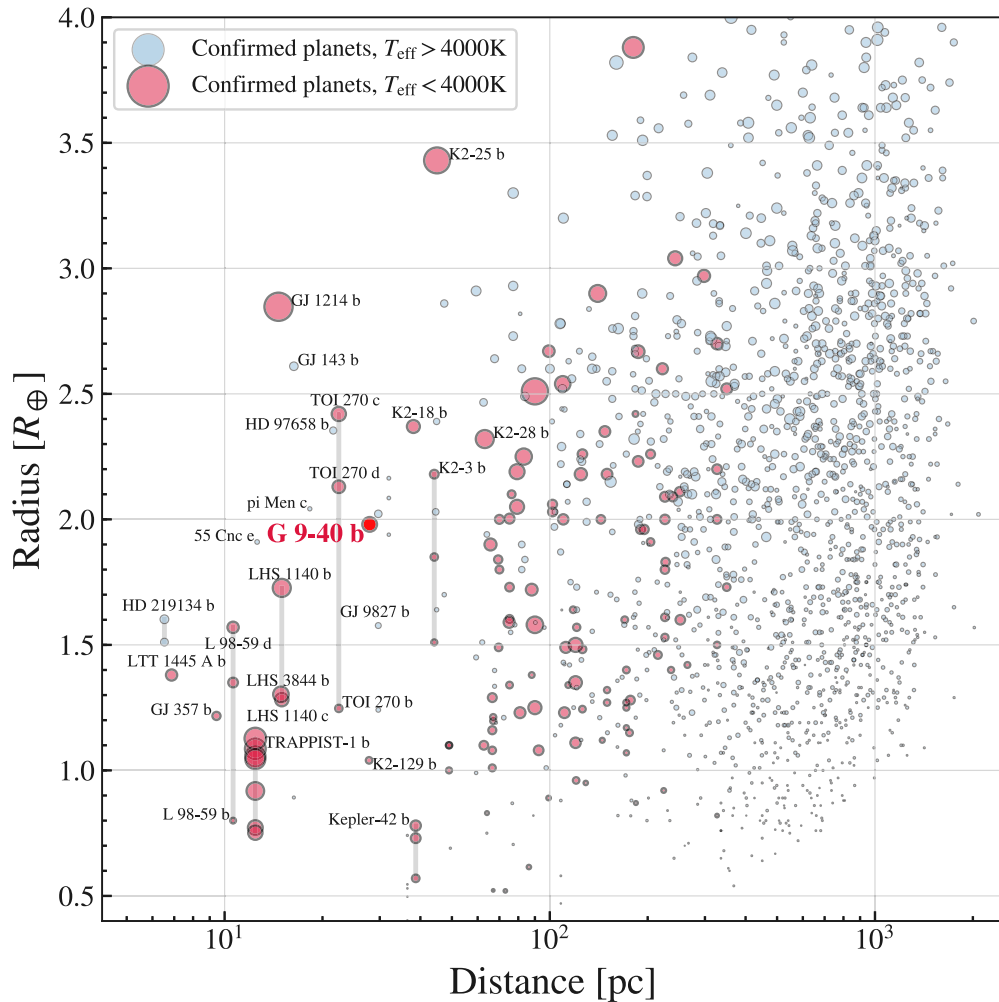


Figure 12. Planet radius as a function of distance for currently known planets from the NASA Exoplanet Archive (2019 June, in addition to the newly discovered M3 system L 98-59 from Cloutier et al. 2019) with radii between $0.5R_{\oplus} < R < 4.0R_{\oplus}$. G 9-40b (highlighted in bold red font) is the second-closest planet discovered by *K2* to date. M dwarf planets are shown in red, while planets around earlier-type stars are shown in blue. The size of the points is proportional to the transit depth of the planet. Names of a few select nearby systems are shown. Gray lines connect planets in the same system for a few select M dwarf systems. This plot is inspired by Figure 4 in Vanderspek et al. (2019).

Kempton et al. (2018) argue that a large sample of sub-Neptune planets is needed for precise atmospheric characterization, to adequately study the high degree of diversity expected for their atmospheric compositions.

7. Summary

We validate the discovery of a sub-Neptune-sized $R \sim 2R_{\oplus}$ planet orbiting the nearby ($d = 27.9$ pc) high-proper-motion M2.5 dwarf G 9-40, discovered using photometric data from the *K2* mission. G 9-40 is the second closest transiting planetary system discovered by the *K2* mission to date. We validate the planetary origin of the *K2* transits using ground-based AO imaging using the ShaneAO system on the Lick 3 m Telescope, precision diffuser-assisted narrowband (37 nm wide filter centered at 857 nm) transit photometry using the ARCTIC imager at the ARC 3.5 m Telescope at APO, and precision NIR radial velocities from the HPF spectrograph on the 10 m HET.

With its large transit depth of ~ 3500 ppm and the brightness of its host star, G 9-40b is a promising target for transmission spectroscopic observations. Using the transmission spectroscopic metric of Kempton et al. (2018), we show that G 9-40b is

currently among the best small ($R < 4R_{\oplus}$) M dwarf planets for transmission spectroscopy with *JWST*. Using the HPF radial velocities, we place an upper bound of $< 11.7M_{\oplus}$ at 3σ on its mass. We predict the mass of G 9-40b using both *Forecaster* and the *MRExo* MR forecasting tool kits, resulting in mass estimates of $M = 5.04^{+3.79}_{-1.91}M_{\oplus}$ and $M = 3.94^{+11.5}_{-3.3}M_{\oplus}$, respectively. The expected mass from *Forecaster* translates to a semiamplitude of $K \sim 4 \text{ m s}^{-1}$, making G 9-40b measurable with current precision RV facilities in the red-optical and the NIR. We urge further ground-based RV follow-up work to measure the mass of G 9-40b. A mass measurement of G 9-40b will provide valuable insights into the exoplanet MR relationship of M dwarf planets, along with enabling future precise transmission spectroscopic analysis.

We thank the anonymous referee for a thoughtful reading of the manuscript and for useful suggestions and comments that made for a clearer manuscript. This work was partially supported by funding from the Center for Exoplanets and Habitable Worlds. The Center for Exoplanets and Habitable Worlds is supported by the Pennsylvania State University, the

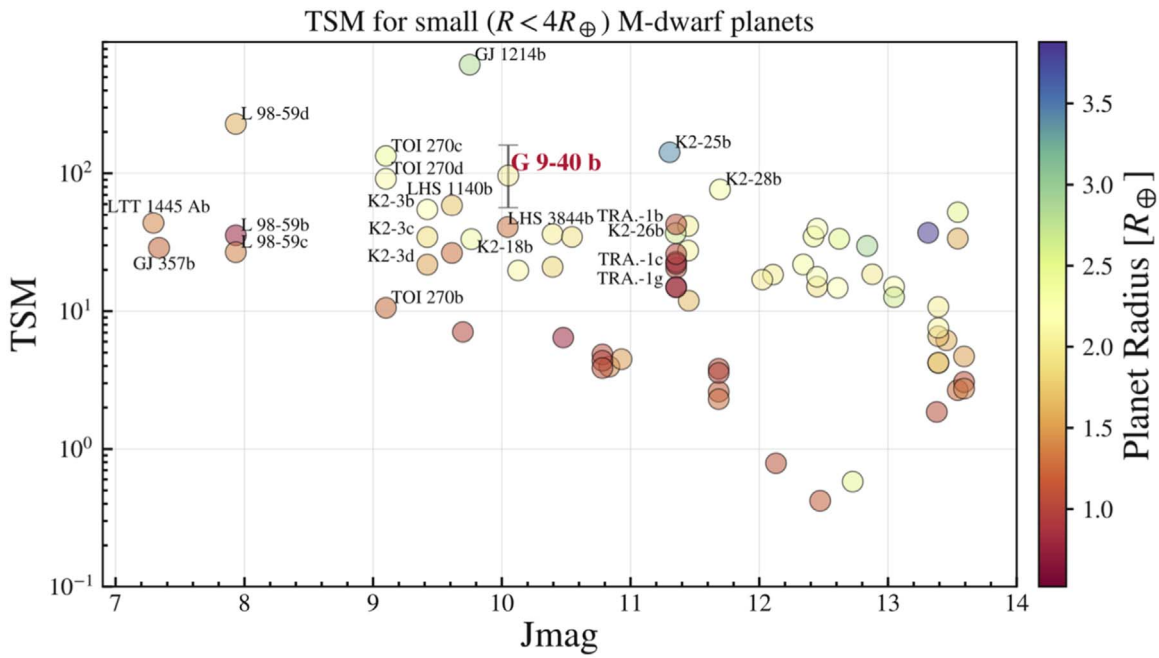


Figure 13. TSM from Kempton et al. (2018) as a function of J magnitude for currently known small ($R < 4R_{\oplus}$) M dwarf planets, with a subset of the planetary systems highlighted. G 9-40b is currently among the top M dwarf planets for transmission spectroscopic observations with this metric in this radius bin with a TSM metric of $TSM = 96_{-41}^{+64}$ (assuming the predicted `Forecaster` mass posterior), exceeding the $TSM > 90$ threshold for high-quality atmospheric targets suggested in Kempton et al. (2018). The TRAPPIST-1 planets are denoted by “TRA-1.”

Eberly College of Science, and the Pennsylvania Space Grant Consortium. This work was supported by NASA Headquarters under the NASA Earth and Space Science Fellowship Program through grants NNX16AO28H and 80NSSC18K1114. We acknowledge support from NSF grants AST-1006676, AST-1126413, AST-1310885, AST-1517592, AST-1310875, the NASA Astrobiology Institute (NAI; NNA09DA76A), and PSARC in our pursuit of precision radial velocities in the NIR. Computations for this research were performed on the Pennsylvania State University’s Institute for CyberScience Advanced CyberInfrastructure (ICS-ACI). We acknowledge support from the Heising-Simons Foundation via grant 2017-0494.

These results are based on observations obtained with the Habitable-zone Planet Finder Spectrograph on the Hobby–Eberly Telescope. We thank the resident astronomers and telescope operators at the HET for the skillful execution of our observations with HPF. The Hobby–Eberly Telescope is a joint project of the University of Texas at Austin, the Pennsylvania State University, Ludwig-Maximilians-Universität München, and Georg-August Universität Göttingen. The HET is named in honor of its principal benefactors, William P. Hobby and Robert E. Eberly. The HET collaboration acknowledges the support and resources from the Texas Advanced Computing Center.

These results are based on observations obtained with the 3 m Shane Telescope at Lick Observatory. The authors thank the Shane telescope operators, AO operators, and laser operators for their assistance in obtaining these data. These results are based on observations obtained with the Apache Point Observatory 3.5 m telescope, which is owned and operated by the Astrophysical Research Consortium. We wish

to thank the APO 3.5 m telescope operators for their assistance in obtaining these data.

This paper includes data collected by the *Kepler* telescope. The *Kepler* and *K2* data presented in this paper were obtained from the Mikulski Archive for Space Telescopes (MAST). The Space Telescope Science Institute is operated by the Association of Universities for Research in Astronomy, Inc., under NASA contract NAS5-26555. Support for MAST for non-*HST* data is provided by the NASA Office of Space Science via grant NNX09AF08G and by other grants and contracts. Funding for the *K2* Mission is provided by the NASA Science Mission directorate. This research made use of the NASA Exoplanet Archive, which is operated by the California Institute of Technology, under contract with the National Aeronautics and Space Administration under the Exoplanet Exploration Program. This work has made use of the VALD database, operated at Uppsala University, the Institute of Astronomy RAS in Moscow, and the University of Vienna. This work has made use of data from the European Space Agency (ESA) mission *Gaia* (<https://www.cosmos.esa.int/gaia>), processed by the *Gaia* Data Processing and Analysis Consortium (DPAC, <https://www.cosmos.esa.int/web/gaia/dpac/consortium>). Funding for the DPAC has been provided by national institutions, in particular the institutions participating in the *Gaia* Multilateral Agreement.

Facilities: *K2*, *Gaia*, ARCTIC/ARC 3.5 m, ShaneAO/Lick 3 m, HPF/HET 10 m.

Software: AstroImageJ (Collins et al. 2017), astroplan (Morris et al. 2018), astropy (Astropy Collaboration et al. 2013), astroquery (Ginsburg et al. 2018), barycorrpy (Kanodia & Wright 2018), batman (Kreidberg 2015), corner.py (Foreman-Mackey 2016), celerite (Foreman-Mackey et al. 2017), emcee (Foreman-Mackey et al. 2013),

everest (Luger et al. 2018), EXOFASTv2 (Eastman 2017), GNU parallel (Tange 2015), iDiffuse (Stefansson et al. 2018b), Jupyter (Kluyver et al. 2016), juliet (Espinoza et al. 2019), matplotlib (Hunter 2007), numpy (Van Der Walt et al. 2011), MC3 (Cubillos et al. 2017), MRExo (Kanodia et al. 2019), pandas (McKinney 2010), pyde (Parviainen 2016), radvel (Fulton et al. 2018), SERVAL (Zechmeister et al. 2018), statsmodels (Seabold et al. 2017), telfit (Gullikson et al. 2014), VESPA (Morton 2012, 2015).

Appendix HPF RV Drifts

HPF has a characteristic sawtooth drift pattern at the $\sim 10\text{--}15\text{ m s}^{-1}$ level throughout a 24 hr period (see Figure 14). This drift pattern is related to the filling of the HPF liquid nitrogen (LN2) tank (Metcalf et al. 2019), which is filled every morning to allow HPF to maintain a stable operating temperature. Although this drift characteristic of HPF has been discussed in detail in Metcalf et al. (2019), we further detail here the RV drift of HPF during the four nights we obtained RV observations of G 9-40, and we discuss the contribution the RV drift makes to the total estimated RV error.

Figure 15 shows the drift of HPF during the four nights we obtained G 9-40 RV observations. The black points in Figure 15 show the RV drift derived from the HPF LFC through the HPF calibration fiber when no star was being observed, but such exposures are taken throughout the night to monitor the drift of HPF through the calibration fiber. The dedicated LFC drift-monitoring exposures all had a fixed exposure time of 106.5 s. The red curve in Figure 15 shows the drift model used to estimate the drift of HPF between the black points. The timing of the eight exposures of G 9-40 we obtained is denoted by the orange vertical lines in Figure 15. From Figure 15 we see no major deviations from a linear drift behavior.

We calculate the HPF drift model (red curves in Figures 14 and 15) in three steps for a given night:

1. First, for a given night, the overall least-squares slope s of the drift curve is estimated from the as-measured RV drifts d_1, d_2, \dots, d_N , where N is the number of HPF LFC calibration observations taken that night through the HPF calibration fiber.
2. Second, N independent drift estimates d'_1, d'_2, \dots, d'_N for the target observation are estimated by linearly extrapolating all of the individual LFC drift estimates d_i to the flux-weighted midpoint of the target observation T , using the following formula:

$$d'_i = s(T - t_i) + d_i, \quad (6)$$

for all $i \in \{1, 2, \dots, N\}$.

3. Lastly, the final drift value $D(T)$ for our observation obtained at flux-weighted time T is estimated by taking a weighted average of the N independent drift values d'_1, d'_2, \dots, d'_N , where

$$D = \frac{\sum_i^N w_i d'_i}{\sum_i^N w_i}, \quad (7)$$

where the weights, $w_i = (T - t_i)^{-2}$, ensure that drift values closest in time to our observation carry the most weight in the average value.

Since our drifts are dominated by systematics (Metcalf et al. 2019) instead of photon noise, we estimate the error of each drift measurement empirically in two steps. First, we estimate the error on each LFC-measured drift point using a leave-one-out approach. We drop the measurement whose error we want to estimate and then estimate the drift at that epoch using our drift model (Equations (6) and (7)). We then compute the difference between the estimated drift and our measured drift to obtain an estimate of the error of that single LFC measurement. Second, we treat these errors as independent and propagate this through the weighted-average formula to estimate the drift at the epoch of G 9-40 observations. This leads to drift error estimates $< 30\text{ cm s}^{-1}$ for all of our G 9-40 observations, which we add in quadrature to our estimated RV errors. Our drift errors for each G 9-40 observation are listed in Table 6.

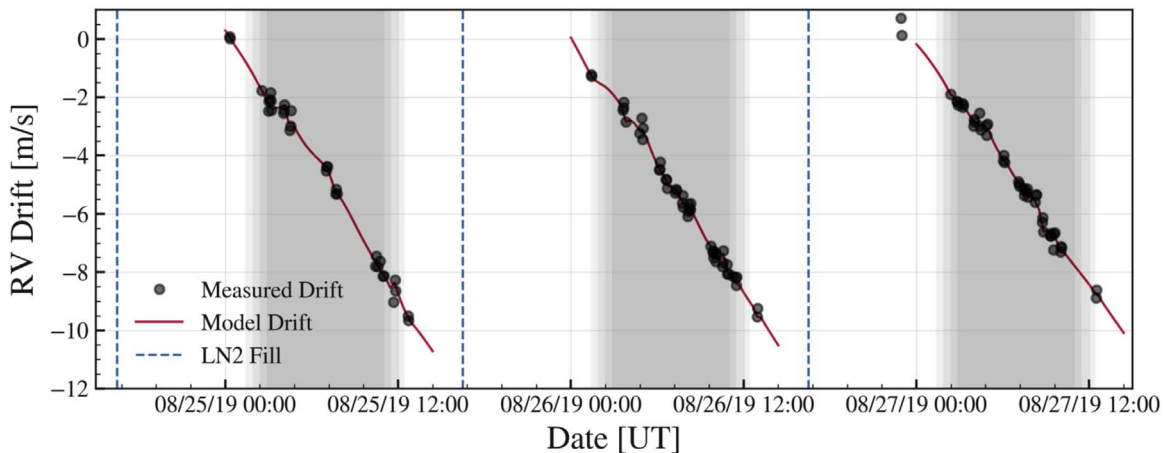


Figure 14. HPF RV drift as measured by the HPF LFC over three consecutive nights (gray shaded regions), to illustrate the characteristic sawtooth drift behavior of HPF, which remains linear throughout a given night, allowing us to precisely model and correct observations without simultaneous LFC observations. The black points show the RV drift as measured by the HPF LFC through the HPF calibration fiber. The red curve shows the RV drift model (see discussion in text), and the blue dashed lines show the timing of the HPF LN2 fills.

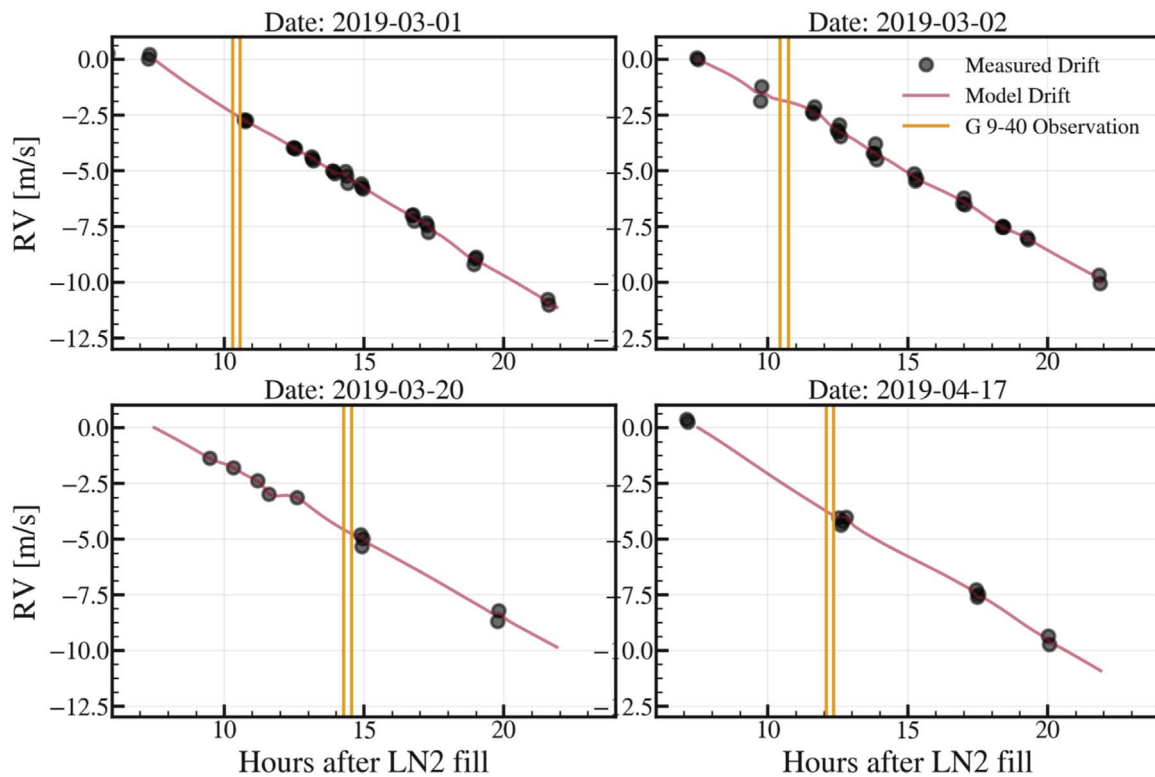


Figure 15. Nightly drift of HPF during the observations of G 9-40. The black points show when HPF LFC calibration observations were obtained for the drift estimates used in this work. The red curve denotes the HPF model drift used to estimate HPF drifts throughout the night. The orange vertical lines show the times when G 9-40 observations were taken.

ORCID iDs

Gudmundur Stefansson <https://orcid.org/0000-0001-7409-5688>
 Caleb Cañas <https://orcid.org/0000-0003-4835-0619>
 John Wisniewski <https://orcid.org/0000-0001-9209-1808>
 Paul Robertson <https://orcid.org/0000-0003-0149-9678>
 Suvrath Mahadevan <https://orcid.org/0000-0001-9596-7983>
 Shubham Kanodia <https://orcid.org/0000-0001-8401-4300>
 Chad F. Bender <https://orcid.org/0000-0003-4384-7220>
 William Cochran <https://orcid.org/0000-0001-9662-3496>
 Michael Endl <https://orcid.org/0000-0002-7714-6310>
 Eric B. Ford <https://orcid.org/0000-0001-6545-639X>
 Samuel Halverson <https://orcid.org/0000-0003-1312-9391>
 Leslie Hebb <https://orcid.org/0000-0003-1263-8637>
 Brett Morris <https://orcid.org/0000-0003-2528-3409>
 Joe P. Ninan <https://orcid.org/0000-0001-8720-5612>
 Arpita Roy <https://orcid.org/0000-0001-8127-5775>
 Christian Schwab <https://orcid.org/0000-0002-0091-7105>
 Steinn Sigurdsson <https://orcid.org/0000-0002-8187-1144>
 Ryan Terrien <https://orcid.org/0000-0002-4788-8858>
 Jason T. Wright <https://orcid.org/0000-0001-6160-5888>

References

Akeson, R. L., Chen, X., Ciardi, D., et al. 2013, *PASP*, **125**, 989
 Allard, F., Homeier, D., & Freytag, B. 2012, *RSPTA*, **370**, 2765
 Anglada-Escudé, G., & Butler, R. P. 2012, *ApJS*, **200**, 15
 Angus, R., Morton, T., Aigrain, S., Foreman-Mackey, D., & Rajpaul, V. 2018, *MNRAS*, **474**, 2094
 Astropy Collaboration, Robitaille, T. P., Tollerud, E. J., et al. 2013, *A&A*, **558**, A33
 Batalha, N. E., Kempton, E. M.-R., & Mbarek, R. 2017, *ApJL*, **836**, L5

Batalha, N. E., & Line, M. R. 2017, *AJ*, **153**, 151
 Bleic, J., Harrington, J., Madhusudhan, N., et al. 2013, *ApJ*, **779**, 5
 Bodenheimer, P., Lin, D. N. C., & Mardling, R. A. 2001, *ApJ*, **548**, 466
 Borucki, W. J., Koch, D., Basri, G., et al. 2010, *Sci*, **327**, 977
 Brahm, R., Jordán, A., & Espinoza, N. 2017, *PASP*, **129**, 034002
 Charbonneau, D., Berta, Z. K., Irwin, J., et al. 2009, *Natur*, **462**, 891
 Chen, J., & Kipping, D. 2017, *ApJ*, **834**, 17
 Choi, J., Dotter, A., Conroy, C., et al. 2016, *ApJ*, **823**, 102
 Clough, S. A., Shephard, M. W., Mlawer, E. J., et al. 2005, *JQSTRT*, **91**, 233
 Cloutier, R., Astudillo-Defru, N., Bonfils, X., et al. 2019, *A&A*, **629**, A111
 Collins, K. A., Kielkopf, J. F., Stassun, K. G., & Hessman, F. V. 2017, *AJ*, **153**, 77
 Cowan, N. B., Greene, T., Angerhausen, D., et al. 2015, *PASP*, **127**, 311
 Crossfield, I. J. M., & Kreidberg, L. 2017, *AJ*, **154**, 261
 Cubillos, P., Harrington, J., Loredó, T. J., et al. 2017, *AJ*, **153**, 3
 Cutri, R. M., Skrutskie, M. F., van Dyk, S., et al. 2003, *yCat*, **2246**, 0
 Cutri, R. M., Wright, E. L., Conrow, T., et al. 2014, *yCat*, **2328**, 0
 Czekala, I., Andrews, S. M., Mandel, K. S., Hogg, D. W., & Green, G. M. 2015, *ApJ*, **812**, 128
 Dotter, A. 2016, *ApJS*, **222**, 8
 Dressing, C. D., Hardegree-Ullman, K., Schlieder, J. E., et al. 2019, *AJ*, **158**, 87
 Dressing, C. D., Vanderburg, A., Schlieder, J. E., et al. 2017, *AJ*, **154**, 207
 Eastman, J. 2017, EXOFASTv2: Generalized Publication-quality Exoplanet Modeling Code, Version 2, Astrophysics Source Code Library, ascl:1710.003
 Espinoza, N., Kossakowski, D., & Brahm, R. 2019, *MNRAS*, **490**, 2262
 Fischer, D. A., Anglada-Escudé, G., Arriagada, P., et al. 2016, *PASP*, **128**, 066001
 Ford, E. B. 2006, *ApJ*, **642**, 505
 Foreman-Mackey, D. 2016, *JOSS*, **1**, 24
 Foreman-Mackey, D., Agol, E., Ambikasaran, S., & Angus, R. 2017, *AJ*, **154**, 220
 Foreman-Mackey, D., Hogg, D. W., Lang, D., & Goodman, J. 2013, *PASP*, **125**, 306
 Fulton, B. J., Petigura, E. A., Blunt, S., & Sinukoff, E. 2018, *PASP*, **130**, 044504
 Fulton, B. J., Petigura, E. A., Howard, A. W., et al. 2017, *AJ*, **154**, 109
 Furlan, E., Ciardi, D. R., Everett, M. E., et al. 2017, *AJ*, **153**, 71
 Gaia Collaboration, Brown, A. G. A., Vallenari, A., et al. 2018, *A&A*, **616**, 1

- Ginsburg, A., Sipocz, B., Parikh, M., et al. 2018, *astropy/astroquery*: v0.3.7 Release, Zenodo, doi:[10.5281/zenodo.1160627](https://doi.org/10.5281/zenodo.1160627)
- Goldreich, P., & Soter, S. 1966, *Icar*, **5**, 375
- Gray, D. F. 1992, *The Observation and Analysis of Stellar Photospheres* (Cambridge: Cambridge Univ. Press)
- Green, G. M., Schlafly, E. F., Zucker, C., Speagle, J. S., & Finkbeiner, D. P. 2019, *ApJ*, **887**, 93
- Gullikson, K., Dodson-Robinson, S., & Kraus, A. 2014, *AJ*, **148**, 53
- Günther, M. N., Pozuelos, F. J., Dittmann, J. A., et al. 2019, *NatAs*, **3**, 1099
- Henden, A. A., Levine, S., Terrell, D., & Welch, D. L. 2015, AAS Meeting, **225**, 336.16
- Howe, A. R., Burrows, A., & Deming, D. 2017, *ApJ*, **835**, 96
- Howell, S. B., Sobeck, C., Haas, M., et al. 2014, *PASP*, **126**, 398
- Huber, D., Bryson, S. T., Haas, M. R., et al. 2016, *ApJS*, **224**, 2
- Huehnerhoff, J., Ketzbeck, W., Bradley, A., et al. 2016, *Proc. SPIE*, **9908**, 99085H
- Hunter, J. D. 2007, *CSE*, **9**, 90
- Kanodia, S., Wolfgang, A., Stefansson, G. K., Ning, B., & Mahadevan, S. 2019, *ApJ*, **882**, 38
- Kanodia, S., & Wright, J. 2018, *RNAAS*, **2**, 4
- Kaplan, K. F., Bender, C. F., Terrien, R., et al. 2018, in ASP Conf. Ser. 523, *Astronomical Data Analysis Software and Systems XXVIII*, ed. P. J. Teuben et al. (San Francisco, CA: ASP), 567
- Kempton, E. M.-R., Bean, J. L., Louie, D. R., et al. 2018, *PASP*, **130**, 114401
- Kipping, D. M. 2010, *MNRAS*, **408**, 1758
- Kipping, D. M. 2013, *MNRAS*, **435**, 2152
- Kluyver, T., Ragan-Kelley, B., Pérez, F., et al. 2016, in *Positioning and Power*, ed. F. Loizides & B. Schmidt (Amsterdam: IOS Press), 87
- Kovács, G., Zucker, S., & Mazeh, T. 2002, *A&A*, **391**, 369
- Kreidberg, L. 2015, *PASP*, **127**, 1161
- Lépine, S., & Shara, M. M. 2005, *AJ*, **129**, 1483
- Louie, D. R., Deming, D., Albert, L., et al. 2018, *PASP*, **130**, 044401
- Luger, R., Agol, E., Kruse, E., et al. 2016, *AJ*, **152**, 100
- Luger, R., Kruse, E., Foreman-Mackey, D., Agol, E., & Saunders, N. 2018, *AJ*, **156**, 99
- Mahadevan, S., Ramsey, L., Bender, C., et al. 2012, *Proc. SPIE*, **8446**, 84461S
- Mahadevan, S., Ramsey, L. W., Terrien, R., et al. 2014, *Proc. SPIE*, **9147**, 91471G
- Mandel, K., & Agol, E. 2002, *ApJL*, **580**, L171
- Mann, A. W., Gaidos, E., Mace, G. N., et al. 2016, *ApJ*, **818**, 46
- McKinney, W. 2010, in *Proc. 9th Python in Science Conf.*, ed. S. van der Walt & J. Millman (Austin, TX: SciPy), 51
- McQuillan, A., Mazeh, T., & Aigrain, S. 2013, *ApJL*, **775**, L11
- Metcalf, A. J., Anderson, T., Bender, C. F., et al. 2019, *Optic*, **6**, 233
- Morris, B. M., Tollerud, E., Sipocz, B., et al. 2018, *AJ*, **155**, 128
- Morton, T. D. 2012, *ApJ*, **761**, 6
- Morton, T. D. 2015, VESPA: False Positive Probabilities Calculator, Version 0.5.1, Astrophysics Source Code Library, ascl:[1503.011](https://ascl.net/1503.011)
- Nelder, J., & Mead, R. 1965, *CompJ*, **7**, 308
- Ninan, J. P., Bender, C. F., Mahadevan, S., et al. 2018, *Proc. SPIE*, **10709**, 107092U
- Ninan, J. P., Mahadevan, S., Stefansson, G., et al. 2019, arXiv:[1903.06614](https://arxiv.org/abs/1903.06614)
- Ning, B., Wolfgang, A., & Ghosh, S. 2018, *ApJ*, **869**, 5
- Parviainen, H. 2016, PyDE: v1.5, Zenodo, doi:[10.5281/zenodo.45602](https://doi.org/10.5281/zenodo.45602)
- Pepper, J., Stanek, K. Z., Pogge, R. W., et al. 2008, *AJ*, **135**, 907
- Reid, I. N., Cruz, K. L., Allen, P., et al. 2004, *AJ*, **128**, 463
- Reiners, A., Joshi, N., & Goldman, B. 2012, *AJ*, **143**, 93
- Reiners, A., Zechmeister, M., & Caballero, J. A. 2018, *A&A*, **612**, A49
- Ribas, I., Tuomi, M., Reiners, A., et al. 2018, *Natur*, **563**, 365
- Ryabchikova, T., Piskunov, N., Kurucz, R. L., et al. 2015, *PhysS*, **90**, 054005
- Seabold, S., Perktold, J., Fulton, C., et al. 2017, *statsmodels/statsmodels*, Version 0.8.0 Release, Zenodo, doi:[10.5281/zenodo.275519](https://doi.org/10.5281/zenodo.275519)
- Seager, S., & Mallén-Ornelas, G. 2003, *ApJ*, **585**, 1038
- Shetrone, M., Cornell, M. E., Fowler, J. R., et al. 2007, *PASP*, **119**, 556
- Srinath, S., McGurk, R., Rockosi, C., et al. 2014, *Proc. SPIE*, **9148**, 91482Z
- Stefansson, G., Hearty, F., Robertson, P., et al. 2016, *ApJ*, **833**, 175
- Stefansson, G., Li, Y., Mahadevan, S., et al. 2018a, *AJ*, **156**, 266
- Stefansson, G., Mahadevan, S., Hebb, L., et al. 2017, *ApJ*, **848**, 9
- Stefansson, G., Mahadevan, S., Wisniewski, J., et al. 2018b, *Proc. SPIE*, **10702**, 1070250
- Tange, O. 2015, GNU Parallel 20150322 ('Hellwig'), Zenodo, doi:[10.5281/zenodo.16303](https://doi.org/10.5281/zenodo.16303)
- Tinetti, G., Drossart, P., Eccleston, P., et al. 2016, *Proc. SPIE*, **9904**, 99041X
- Torres, G., Fischer, D. A., Sozzetti, A., et al. 2012, *ApJ*, **757**, 161
- Van Der Walt, S., Colbert, S. C., & Varoquaux, G. 2011, *CSE*, **13**, 22
- Vanderspek, R., Huang, C. X., Vanderburg, A., et al. 2019, *ApJL*, **871**, L24
- Weiss, L. M., & Marcy, G. W. 2014, *ApJL*, **783**, L6
- Wolfgang, A., Rogers, L. A., & Ford, E. B. 2016, *ApJ*, **825**, 19
- Wright, J. T., & Eastman, J. D. 2014, *PASP*, **126**, 838
- Wright, J. T., & Robertson, P. 2017, *RNAAS*, **1**, 51
- Yee, S. W., Petigura, E. A., & von Braun, K. 2017, *ApJ*, **836**, 77
- Yu, L., Crossfield, I. J. M., Schlieder, J. E., et al. 2018, *AJ*, **156**, 22
- Zacharias, N., Urban, S. E., Zacharias, M. I., et al. 2004, *AJ*, **127**, 3043
- Zechmeister, M., Reiners, A., Amado, P. J., et al. 2018, *A&A*, **609**, A12